## PHYS 6751 Laboratory: *Characterization of a Foil via Rutherford Backscattering*

Lab overview:

- *Objective:* Characterize the composition and thickness of a foil by comparing $\alpha$ spectra from Rutherford backscattering (RBS) measurements to RBS calculations.
- *Gain familiarity with:* $\alpha$ spectroscopy, complex vacuum systems, low-energy particle accelerator experiments, nuclear scattering
- *Report style:* Physical Review C (PRC)

Brief description:

Over the past century Rutherford scattering has transformed from a tool for fundamental science, providing the first direct evidence for an atomic nucleus, to a standard technique for the characterization of thin films. This technique relies on low-energy particle accelerators to scatter light nuclei at ~MeV energies off of ~micron-scale thin films, which are detected at various angles using silicon detectors. Comparing measured spectra to cross section calculations enables the material composition and thickness to be extracted, providing necessary information for industrial applications as well as fundamental nuclear physics research.

In this experiment we will determine the thickness and composition of a foil using the RBS set-up at the Edwards Accelerator Lab (EAL). The 4.5MV tandem will be used to deliver $^4\text{He}^{2+}$ ions to our foil, mounted with the RBS chamber in the small target room. Signals from silicon detectors, which will be placed at various angles, will be used to determine the differential cross section of elastic scattering of $\alpha$-particles on our foil. Foil characterization is completed by comparing measured spectra to RBS differential scattering cross sections, which are analytically determined.

Expectations for Run-plan:

The run-plan should consist of time-saving calculations and an order of operations. For instance,

- How many angles do we need to measure the RBS spectra at and what are the optimum angles?
- How long do we need to measure at each angle given a nominal beam intensity (e.g. 100nA)?
- How will the information about the target be derived from our measurement?
- Why are we using an $\alpha$-beam as opposed to, say, protons or carbon?
- How will we determine the intensity of our $\alpha$-beam?
- What materials is RBS ideally suited to characterize? What impurities would it be liable to miss and how would you detect those?

- What is the experiment order of operations; what information do we need to collect before beginning the measurement?
- ...of course, other preparatory notes are welcome, so long as they're useful!

**NOTE:** The above examples are suggestions. Please do <u>not</u> feel obligated to have all of them done prior to the lab start. You will be working in a group, so with any luck your partners will have prepared for some different portions of the lab.

<u>Expectations for Lab Report:</u>

The lab report should be a publication-quality paper typeset in the style of Physical Review C. As such, it should include a thorough and balanced description of the experiment motivation, the measurement technique, the data analysis, and the significance of the results.

The reports will be written individually, but your group members should appear as co-authors on the paper. As such, you are free to share calculations and plots. In fact, sharing in this sense is expected, as this is how real experiments work. However, <u>all writing must be your own</u>.

**NOTE:** It is quite possible that the lab contains more work than you could possibly get done during the experiment time allotted. This is OK, as I don't expect you to necessarily complete every single task. However, a reasonable amount of work must be completed and that work must be thoroughly described in an articulate way.

## WARNINGS:

- Be careful with the bias voltage
    - Don't electrocute yourself
    - Don't exceed the maximum bias voltage for the detector
    - Don't apply bias without good vacuum
- Be careful with regards to beam-induced radiation
    - **The accelerator operator is in-charge** and **only** they can give you permission to enter the target room
    - The target room must be "swept" for radioactivity by the operator before others enter the room and it must be "swept" for occupants prior to securing the target room and initiating target bombardment.
- <u>If you aren't sure, ask!</u>

# Appendices

1. Notes on RBS
2. Paper on modern use of RBS

## II. Pre-Experiment Checkout

a). After performing the essential pre-lab preparations, begin to understand the experimental setup. This includes understanding the purpose of each part of the system. The basic layout of the Rutherford scattering experiment is shown in Fig. 1.
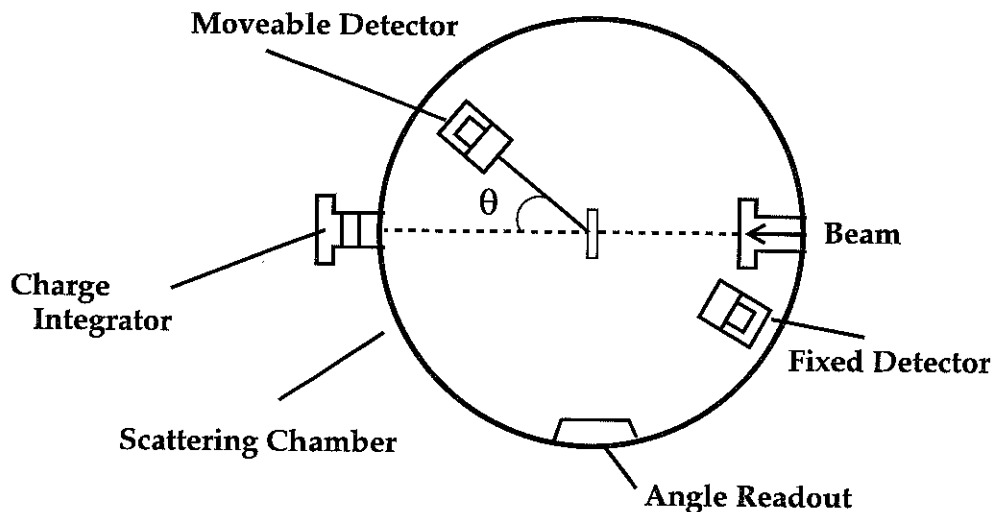


Figure 1: Major components of the Rutherford scattering experiment for this laboratory.

b). Go through the set-up step by step to understand how the electronics are laid out in both the experimental area and the control room. This basic layout and the purpose of each electronics module should be reasonably clear given the experience you have gained in the first part of this course. The manuals for each of the electronics used are available for review. A complete diagram is contained in Fig. 2. Be sure to provide clear and complete documentation in your logbook. Also begin to understand how to operate the data acquisition system and what the defined histograms mean. Make sure you understand where to record the computer dead time for each measurement. This is crucial in order to measure the Rutherford cross section.

c). Make sure you know how to set the angle of the movable silicon detector to the precise angle that you want and that the angle readback makes sense to you. Note that the movable detector is limited to angles in the range from 25° to 150° on one side of the beam and from 250° to 335° on the other.

d). Take measurements of the radial positions of the two silicon detectors. This is required to compute the detector solid angle.

e). Make sure you record the size of the apertures in from of the two silicon detectors. These are required for the solid angle computation.

f). Make sure that you understand how to read out the charge integrator for the alpha beam. This is required in order to determine the number of alphas incident on our gold foil.
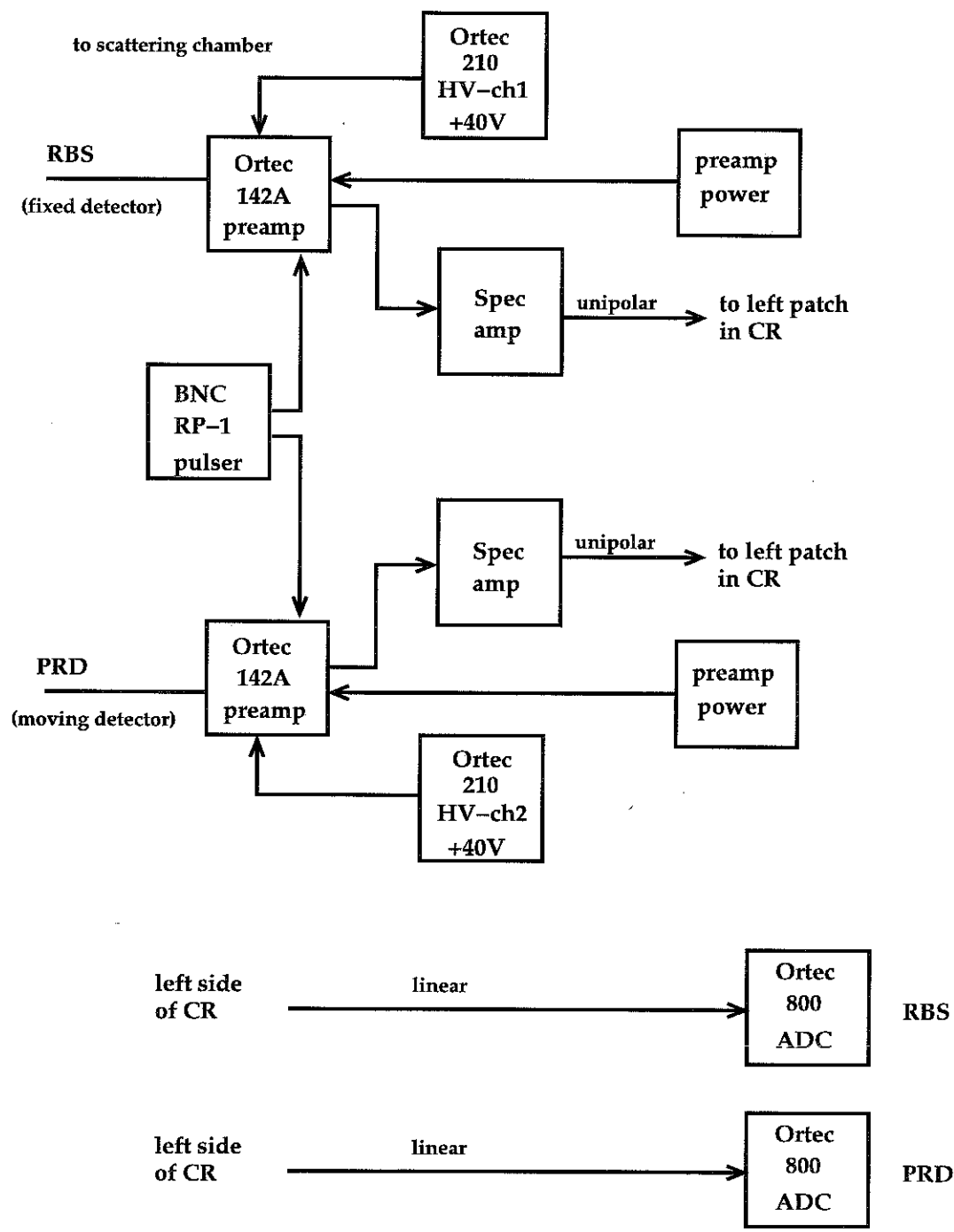
# Electronics Setup



Figure 2: Electronics layout for the Rutherford scattering experiment.

3

g). Make sure you record the thickness of the gold foil (relevant units are $\mu g/cm^2$). This is necessary to compute the cross section.

h). Make sure you know how to set the angle of target (the gold foil). In this experiment we will want to minimize the material traversed by the scattered alpha particle in the gold foil. To accomplish this we will set the angle of the target to be $\theta_{scatt}/2$ for angles $\theta_\alpha \leq 90°$. Here $\theta_{scatt}$ is the defined angle of the silicon detector. For angles larger than 90°, we will set the target angle to be at 0° (i.e. normal to the incident beam flux).

## III. Scattering Cross Section

The scattering of particles is described quantitatively by the differential cross section, $\frac{d\sigma}{d\Omega}$ [1]. We will consider the case when $N_0$ projectiles are incident on a target of uniform thickness described by $n_1$ target nuclei per unit area. The incident projectiles can in principle scatter to any angle with respect to the incident direction. The number of particles scattered into a solid angle $\Delta\Omega$ is given by

$$N_s = \frac{d\sigma}{d\Omega} N_0 \, n_1 \, \Delta\Omega. \tag{1}$$

In general, $\frac{d\sigma}{d\Omega}$ depends on the type of projectile, the type of target, the energy of the projectile, and the scattering angle. Note also that the above formula is technically only exactly true in the limit that $\Delta\Omega \to 0$, due to the fact that $\frac{d\sigma}{d\Omega}$ depends on the scattering angle. The number of scattered particles $N_s$ is directly proportional to $N_0$, $n_1$, and $\Delta\Omega$ as one intuitively expects – in this picture, the differential cross section is the proportionality constant. It is often said that the differential cross section "contains the physics"...

The differential cross section has units of area divided by solid angle. While solid angle is technically dimensionless, we traditionally utilize the units of steradians (sr) to describe it, where $\Delta\Omega = 4\pi$ sr for an entire sphere. In nuclear and particle physics, it is also traditional to use the units of fermis (fm) to describe distances (1 fm=$10^{-13}$ cm) and barns (b) to describe cross sections (1 b=$10^{-24}$ cm$^2$).

## IV. Rutherford Scattering Physics

The Rutherford scattering formula may be derived classically (or quantum-mechanically!) assuming the Coulomb potential between two particles (labeled 0 and 1):

$$U(r) = \frac{Z_0 Z_1 e^2}{4\pi\epsilon_0 r}, \tag{2}$$

where $r$ is the distance between the particles, $Z_0 e$ is the charge of particle 0, $Z_1 e$ is the charge of particle 1, and $\epsilon_0$ is usual electrostatics constant ($\epsilon_0 = 8.854187... \times 10^{-12}$ F/m). The resulting differential cross section is

$$\frac{d\sigma}{d\Omega_{\text{c.m.}}} = \frac{Z_0^2 Z_1^2 e^4}{16(4\pi\epsilon_0)^2 E_{\text{c.m.}}^2} \frac{1}{\sin^4(\theta_{\text{c.m.}}/2)},$$
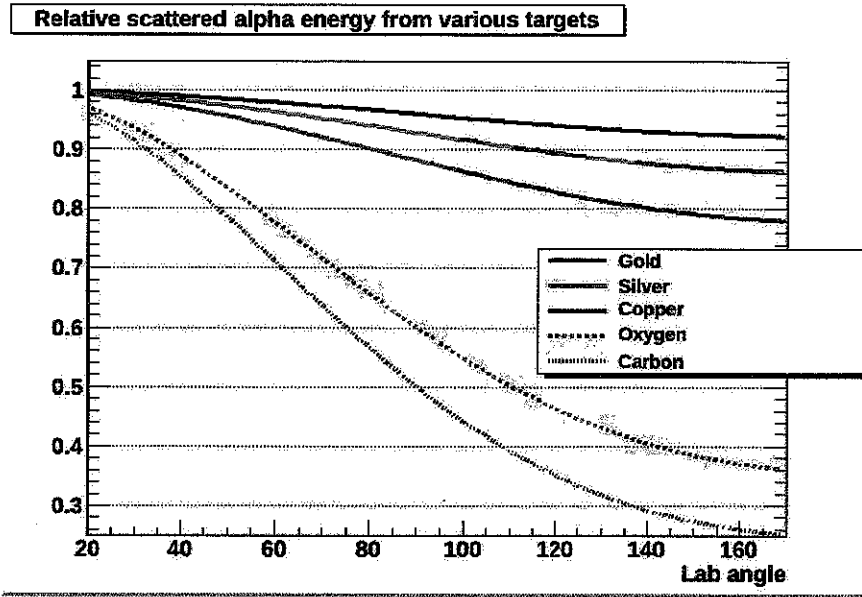
4

Figure 3: Relative scattered energies $(K)$ for several nuclei present in the target foils as a function of laboratory angle.

where $E_{\text{c.m.}}$ and $\theta_{\text{c.m.}}$ are the center-of-mass kinetic energy and scattering angle, respectively. Note that the Rutherford differential cross section diverges as $\theta_{\text{c.m.}} \to 0$ and the total cross section is in fact infinite.

Since we will not be performing the experiment in the center-of-mass coordinate system, there is more work to do. The algebra of changing coordinate systems for the Rutherford formula is non-trivial and is seldom discussed in textbooks. The formulas below are taken from a paper by Sargood [2]. Let's now assume that label 0 refers to the projectile and label 1 refers to the target which is at rest. First we will define

$$K = \left( \frac{M_0 \cos \theta + \sqrt{M_1^2 - M_0^2 \sin^2 \theta}}{M_0 + M_1} \right)^2 , \tag{3}$$

where $M_i$ are the masses and $\theta$ is the *laboratory* scattering angle, where $0°$ is by definition the direction of the incident projectile. We will also define the parameter

$$a = \sqrt{1 - \left( \frac{M_0 \sin \theta}{M_1} \right)^2} . \tag{4}$$

The differential cross section in the laboratory is given by:

$$\frac{d\sigma}{d\Omega} = \frac{Z_0^2 Z_1^2 e^4}{4a(4\pi\epsilon_0)^2 E_0^2} \frac{(a + \cos \theta)^2}{\sin^4 \theta} , \tag{5}$$

where $E_0$ is the kinetic energy of the incident projectile. The energy of the scattered projectile is given by $E_0' = K E_0$. Since $K$ is dependent on both the target mass and the scattering angle, particles scattered from different target nuclei will have different energies; Figure 3 shows the $K$ values for several nuclei as a function of laboratory angle. Note that in the

5

limit $M_0/M_1 \to 0$ ("light" projectile and "heavy" target) we have $K \to 1$ and $a \to 1$ and the lab system is also the center-of-mass system – one can also verify that the differential cross section formulas are equivalent in this limit using the trig identity

$$\frac{1+\cos\theta}{\sin^2\theta} = \frac{1}{2\sin^2(\theta/2)}. \tag{6}$$

It is convenient to expand Eqs. (4) and (5) in powers of $M_0/M_1$; the result is

$$\frac{d\sigma}{d\Omega} = \frac{Z_0^2 Z_1^2 e^4}{16(4\pi\epsilon_0)^2 E_0^2} \left[ \frac{1}{\sin^4(\theta/2)} - 2\left(\frac{M_0}{M_1}\right)^2 \right] + O\left[\left(\frac{M_0}{M_1}\right)^4\right]. \tag{7}$$

The fundamental constants can be inserted as follows

$$\frac{e^4}{(4\pi\epsilon_0)^2} = \left(\frac{e^2}{4\pi\epsilon_0\hbar c}\right)^2 (\hbar c)^2 \tag{8}$$

$$= \left(\frac{1}{137.036}\right)^2 \times (197.327 \text{ MeV-fm})^2 \times \left(\frac{10 \text{ mb}}{\text{fm}^2}\right) \tag{9}$$

$$= 20.735 \text{ mb-MeV}^2 \tag{10}$$

to yield "nuclear physics" units. The final formula is

$$\frac{d\sigma}{d\Omega} = 1.296 \left(\frac{\text{mb-MeV}^2}{\text{sr}}\right) \left(\frac{Z_0 Z_1}{E_0}\right)^2 \left[ \frac{1}{\sin^4(\theta/2)} - 2\left(\frac{M_0}{M_1}\right)^2 \right] \tag{11}$$

which can be used with $E_0$ in MeV to calculate the differential cross section in mb/sr.


# V. Rutherford Scattering Experiment

The experiment will amount to acquiring data at a number of different scattering angles on either side of the incident beam direction. You will record the number of counts in each of our two silicon detectors. The naming convention is to call the fixed detector RBS and the movable detector PRD. In addition to summing up the counts in the ADC spectra, you will have to record the system live time (LT) for each measurement, as well as the real time duration (RT) of each run and the charge integrator value. The counts in the ADC spectra must be multiplied by the ratio RT/LT in order to determine the true number of particles which struck the detector during the real time duration of each run.

In defining $E_0$ for this experiment, use of the incident $\alpha$ beam energy is only an approximation. In general a better approximation is to use the average alpha energy in the target given by:

$$E_{\text{avg}} = \frac{E_i + E_f}{2}, \tag{12}$$

where $E_i$ is the incident alpha energy and $E_f$ is the alpha energy after passing through the gold foil. It would be relevant to compare the sensitivity of the final result with and without this correction.

6

Based on the previous discussion, the measured differential scattering cross section in units of $cm^2/sr$ is given by:

$$\frac{d\sigma}{d\Omega} = \frac{N_s}{N_0 \cdot \Delta\Omega \cdot n_1}$$ (13)

where:

- $N_s$ = the number of detected particles, corrected by the ratio RT/LT.

- $N_0$ = the number of beam particles which impinged on the scattering foil. This quantity is determined from the charge integrator. Remember that we are using a $He^{2+}$ beam when converting the measured number of $\mu C$ to the number of particles.

- $\Delta\Omega$ = the solid angle of the detector (sr). The solid angle is given by $A_c/R^2$, where $A_c$ is the area of the detector (or the defining aperture) and $R$ is the distance of separation between the aperture and the target.

- $n_1$ = the number of target nuclei per $cm^2$. This number will be given to you by your lab instructor.

# Silicon Detectors – Background Information

Semiconductor charged particle detectors have been used extensively in experimental nuclear physics research for over 30 years, and have revolutionized nuclear particle detection. Silicon detectors can be used to measure a wide range of charged particles. This range includes protons and electrons as low as 20 keV up to fission fragments of energy over 100 MeV. The inherent resolution of ion-implanted and surface barrier detectors is surpassed only by magnetic spectrometers. The detector output pulses rise rapidly, hence they are well suited for fast ($\sim$1 ns) timing with coincidence circuitry or time-to-amplitude converters.

The efficiency of silicon charged particle detectors for their active volume is essentially 100%, and their energy vs. pulse height curves are linear over a rather impressive range. They also have good long-term pulse height stability. This is particularly noticed when they are contrasted with scintillation counters, gas proportional counters, or ionization chambers. The high efficiency of these detectors allows for straightforward analysis of cross sections via the extraction of detected particle yields from the accumulated spectra (provided data acquisition/computer dead times are accounted for accurately).

Solid state detectors can be thought of as a solid state ionization detector. When a charged particle enters the depletion region of the detector, it loses energy primarily by making electron-hole pairs in the silicon. For each electron-hole pair that is made, the initial charged particle must lose 3.6 eV. In this experiment we will be measuring alpha particles that have an energy less than 3 MeV. If a 3 MeV alpha particle enters the detector, roughly $8 \times 10^5$ electron-hole pairs will be produced. The detector is reverse-biased and these electron-hole pairs are collected to produce the output pulse of the detector. Since a large number of charge carriers is produced, the statistical variation in the number collected is small and hence very good energy resolution is possible. The "partially depleted" silicon detector used in this experiment has a resolution of roughly 20 keV.

The three main parameters that define a silicon surface-barrier detector are its resolution, active area, and depletion depth. The shape of a typical detector is a circular disk. Thus the active area is simply the area of the face of this disk (provided it is placed normal to the incident flux of radiation). The depletion depth of a detector is synonymous with the sensitive depth of the detector. For any given experiment, this depth must be sufficient to completely stop all the incident charged particles that are to be measured. The detector's ability to do this is dependent upon both the energy and the particle type. Fig. 4 is a range-energy curve for five of the more common charged particles. From it, the maximum depth can be determined for the maximum energy of a particle type. From Fig. 4, note that a 3 MeV alpha particle is completely stopped with about 20 $\mu$m of silicon.
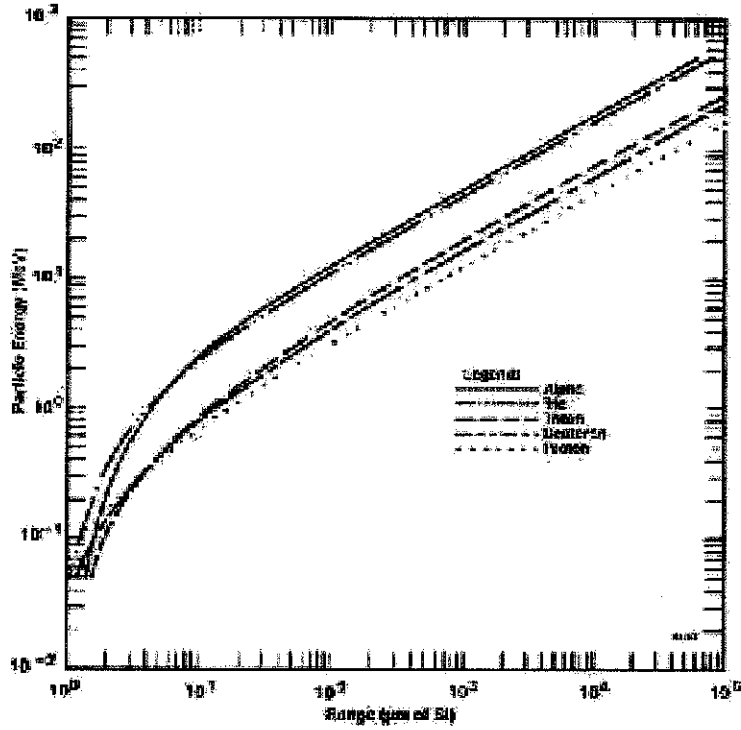
# Acknowledgments

Figure 4: Energy-range curves for charged particles in silicon [3].
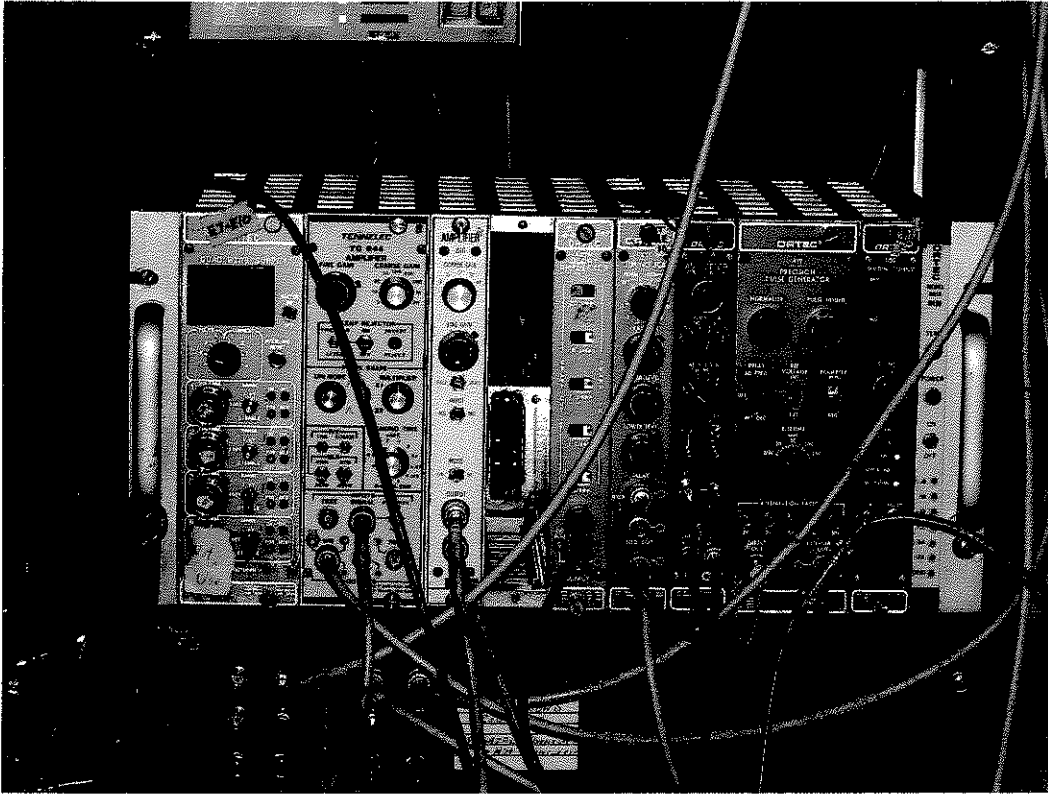
*Science"* by Jerome Duggan (1988).

# References

[1] W.S.C. Williams, *"Nuclear and Particle Physics"* (Clarendon Press, Oxford, 1991).

[2] D.G. Sargood, Physics Reports **93**, No. 2, 61-116 (1982).

[3] C.F. Williamson *et al.*, *"Range of Stopping Power of Chemical Elements for Charged Particles of 0.5 to 500 MeV"*, CEA-R-3042, July 1966.
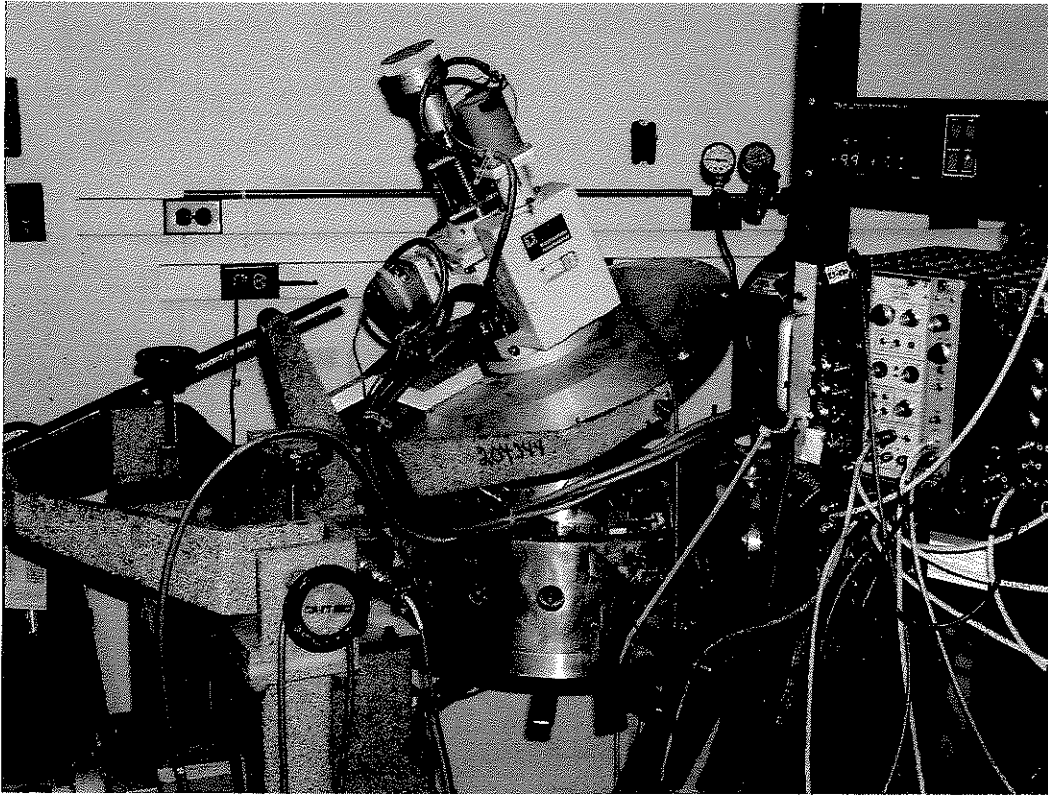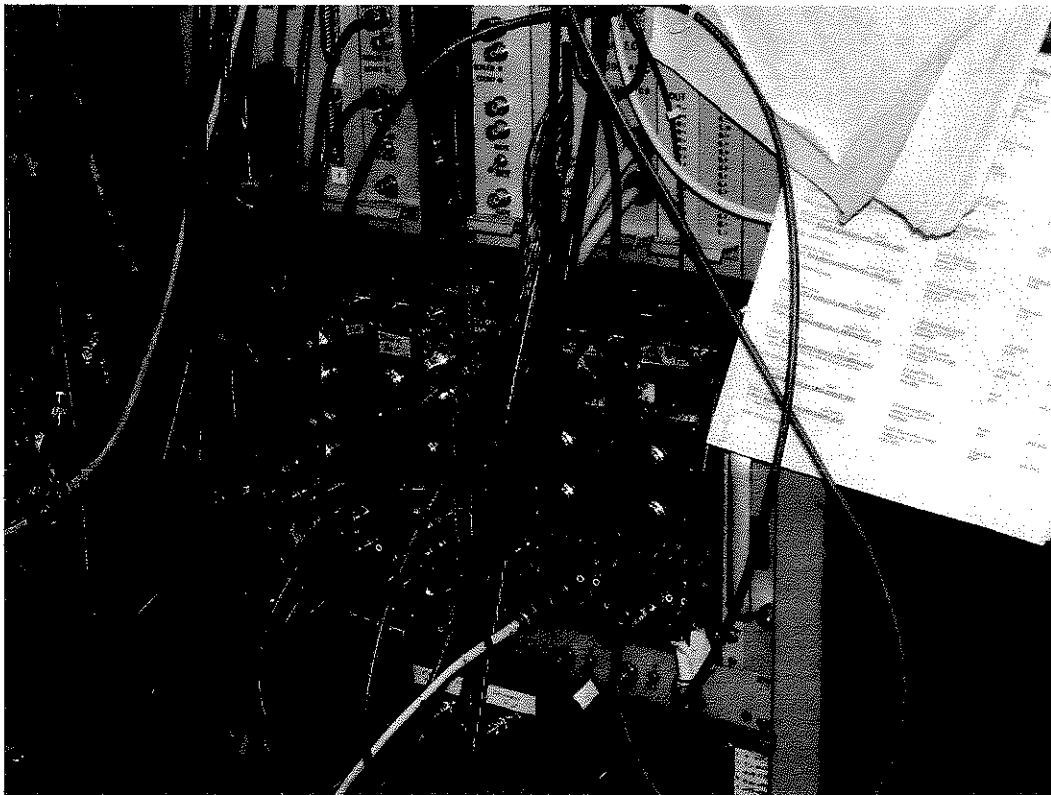
**View of Scattering Chamber (External)**
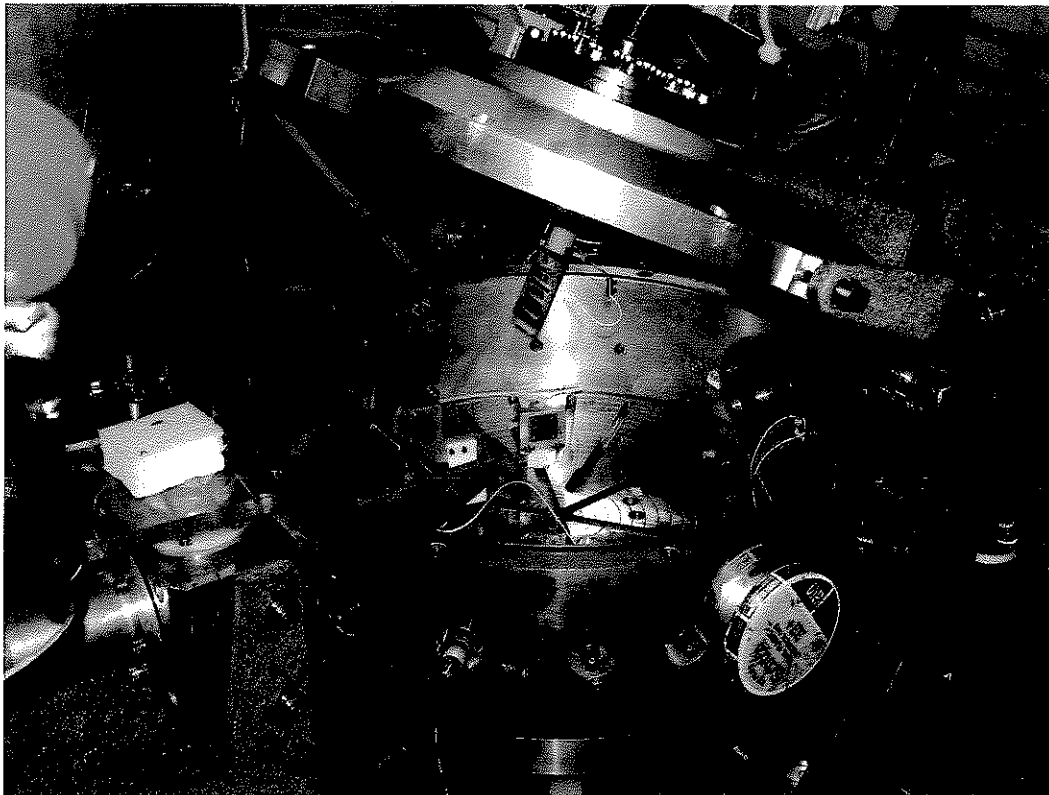


**View of Scattering Chamber (Internal)**

**Experimental Area Electronics**



**Counting Room (CR) Electronics**

11

**Pergamon**

# Rutherford backscattering and nuclear reaction analysis

**L G Earwaker**, *School of Physics and Space Research, University of Birmingham, Edgbaston, Birmingham B15 2TT, UK*

## 1. Introduction

Throughout the 1950s and 1960s nuclear physics research was carried out in an increasingly large number of laboratories around the world, using accelerators producing ion beams with energies of the order of a few MeV. The most commonly used ions were protons, deuterons and alpha particles. As the research developed, a wealth of knowledge was built up on the interaction of energetic ions with all nuclei throughout the periodic table, accelerator energies were extended to higher levels and more complex ions were accelerated. This legacy of accelerator technology and basic nuclear physics information now forms the backbone of the widely used near-surface analytical techniques of Rutherford backscattering (RBS) and nuclear reaction analysis (NRA).

Although Rutherford backscattering and nuclear reactions were first observed soon after the turn of the century[1,2], it was not until forty years later that they were first used by Rubin *et al* in the analysis of materials[3,4]. The rapidly growing need for surface analysis since that time, particularly in the electronic and related industries, has generated much development of energetic-ion-beam analysis techniques to the point where they have graduated from research laboratory developments to routine tools used by high-technology industries. It is now possible to purchase turn-key accelerator analysis facilities providing ions in the energy range up to a few MeV for around $400,000[5], a sum comparable with that required to provide a good quality dynamic SIMS, Auger or ESCA instrument. Taken together, RBS and NRA provide for the measurement of elemental concentrations to a depth of about 10 $\mu$m and with sensitivities in the range down to a fraction of a monolayer or parts per million (atoms) in advantageous cases. The techniques are non destructive, quantitative, sensitive to all elements in the periodic table and, in the case of NRA, isotope specific.

## 2. Energetic ion beam analysis

**2.1. General principles.** When energetic ion beams are incident upon samples of materials they suffer a wide range of interactions. Any one of these interactions can be made the basis of an analysis technique simply by observing that type of interaction and designing the detection system to exclude, as far as possible, the others. This article aims to provide a broad introduction to Rutherford backscattering and nuclear reaction analysis and to illustrate them with a number of specific applications. Readers wishing to explore the topics in greater detail will also find the following, more general references useful. Backscattering spectrometry and channelling have been described by Chu *et al*[6] and Feldman *et al*[7] respectively and an extensive coverage of ion beam analysis of materials is contained in the books by Feldman and Mayer[8] and Bird and Williams[9]. An excellent review of the energetic ion beam analysis of light elements from hydrogen

to neon is contained in the conference proceedings edited by Demortier[10]. Marion and Young[11] have also produced a very useful compilation of graphs and tables of data related to nuclear reaction analysis.

The radiations emitted when energetic ion beams impinge on a sample are illustrated schematically in Figure 1. In Rutherford backscattering and nuclear reaction analysis, emphasis is placed on the scattered and transmitted ion beam, the recoil nuclei and the nuclear reaction products. The sample to be analysed may be 'thick' where the ion beam comes to rest within the bulk of the sample, or 'thin' when the ion beam loses only a small part of its energy in passing through the sample. In some cases nuclear reaction products may penetrate through the sample even though it is thick to the incident beam. This may be the case when nuclear reactions produce very energetic reaction products or the products are neutrons or gamma rays. Figure 2 illustrates the case of the detection of reaction products from thin and thick samples. For the thin sample the incident monoenergetic beam produces a reaction product with well defined energy. Here the energy is defined by the particular interaction and the yield per incident ion is determined by the number of atoms in the path of the beam and the interaction probability or cross-section. In the case of the thick sample, those atoms near the surface will give reaction products of the same energy as from the thin sample. However, as the ion beam penetrates the sample it will lose energy. When a reaction occurs at a depth in the sample, therefore, the reaction product will generally be produced at a reduced energy and it will lose further energy on its way back out of the sample before entering the detector. The contribution of atoms in a thin layer at depth in the sample is therefore correlated with particles
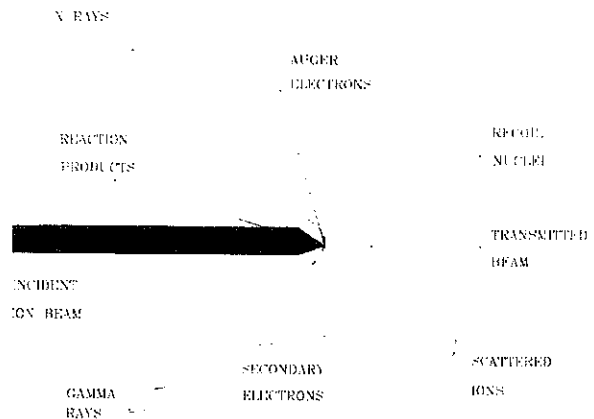


**Figure 1.** A schematic illustration of the radiation processes induced when an energetic ion beam is directed onto a solid material.
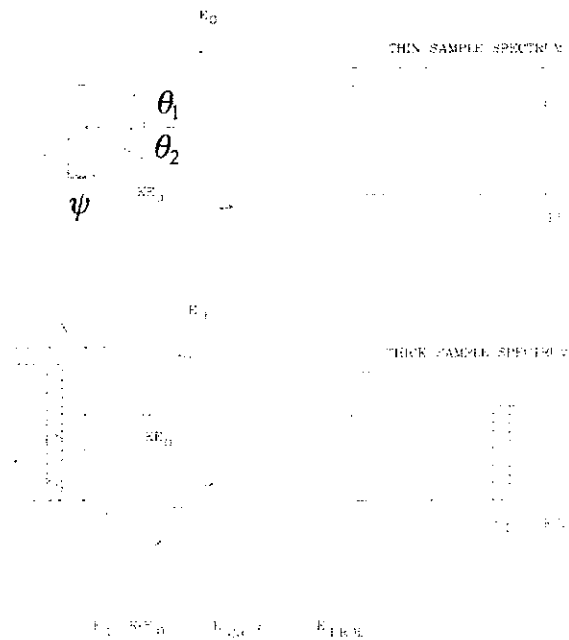
**Figure 2.** The trajectories and energies of energetic ion beam interaction products from the surface and a depth $x$ beneath the surface of a material and the reaction product energy distributions from thin and thick samples.

detected within a given energy element, as shown by the shaded section in Figure 2(b).

**2.2. Energetic ion–atom interactions.** When a beam of energetic ions enters a material, ions in the beam interact with the atoms of the material in various ways, depending on the energy and velocity of the ion. By far the most probable interaction is with orbital electrons of atoms in the material. However, a small fraction of the ions will scatter from atomic nuclei and at higher ion energies an even smaller fraction may interact with nuclei, producing nuclear reactions. All of these processes gradually reduce the energy of the ions and, in the case of nuclear reactions, remove them from the beam completely.

The dominant process, whereby ions lose energy by interaction with electrons to produce excitations and ionization, is known as electronic stopping and is denoted by $(dE/dx)_e$. Because ions are very much heavier than electrons, the fraction of the ion energy transferred in each collision is very small, as is the angular deviation of the ion. An ion beam will therefore slow down in a material in a straight line and, as ions are not removed from the beam, the fluence remains constant along the path. This behaviour has the important consequence that the depth penetrated by an ion can be directly related to its energy at that depth, through the $(dE/dx)_e$ relationship, thus providing the basis for elemental analysis as a function of depth. As the ion slows down, it will reach a velocity comparable with that of inner shell electrons for that ion, with the consequence that electrons may be captured and carried along by the ion. Eventually, as the velocity drops further, electrons will be captured into all shells and the ion will become a neutral atom. At this stage energy loss is no longer by excitation and ionization but by elastic collisions between atoms. The particles involved in these collisions now have much more comparable masses, large energy transfers

become possible in single collisions and large changes in direction of the incident ion are probable. This process is known as nuclear stopping and is denoted by $(dE/dx)_n$. It is this nuclear stopping process that gives rise to sputtering. In this regime it is much more difficult to relate depth with energy or with ion direction, which can introduce complications when heavy ions are used for analysis. For almost all cases of energetic ion beam analysis however, nuclear stopping effects can be ignored. Charge exchange only begins to play a role for ions of energy below about 100 keV per atomic unit and nuclear stopping becomes comparable with electronic stopping at a few keV per atomic mass unit.

The energy loss process in the electronic stopping regime consists of a series of collisions with electrons, each removing a small but different amount of energy from the ion. The energy loss is thus a statistical process and, as a result, ions which initially have the same energy will lose slightly different amounts of energy when passing through the same thickness of material. This process is known as energy straggling. For an ion of charge $Z_1$ passing through a material composed of an element of number density $N$ atoms per unit volume and atomic number $Z_2$, a simple form of the energy straggling, calculated by Bohr, states that the full-width-at-half-maximum of the energy distribution after passing through a thickness of $\Delta x$ is proportional to $[NZ_1^2Z_2\Delta x]^{1/2}$. As an example, a 2 MeV $^4$He beam traversing 0.5 $\mu$m of Si has an energy loss of 123 keV and a straggling of about 7 keV. Clearly, as energy loss is translated into depth, straggling results in an uncertainty in the depth measurement. For heavy ions the straggling increases greatly with mass and charge. In addition, if the velocity of the ion approaches the nuclear stopping regime, large angle scattering introduces an additional uncertainty to the depth scale.

A very small number of ions, perhaps as low as one in every $10^5$ or $10^6$, will approach sufficiently closely to an atomic nucleus to undergo a Coulomb interaction with the nuclear charge. In general, the distance of closest approach will not be short enough for nuclear forces to come into play and the ion will be scattered according to the well known Coulomb scattering laws and with a well defined analytical probability. This process is known as Rutherford scattering. For higher ion energies and, particularly, for low atomic number ions, some of the larger angle collisions will enable the ion to enter the region of the nuclear forces. In these cases the analytical Coulomb scattering probability will be modified by nuclear effects and the probability of interaction can no longer be calculated in a simple manner. Non-Rutherford effects are most severe for light ion/light atom combinations, being particularly evident for protons above a few hundred keV and alpha particles above 2 MeV incident on atoms with atomic number less than 11. In addition to nuclear elastic scattering, an even smaller fraction of the ions may undergo nuclear transformation. In favourable cases, perhaps one ion in $10^8$ will induce a nuclear reaction.

In discussing the interactions of ions with materials, no consideration has yet been given to the structure of the slowing down medium. Very many materials are crystalline in form with highly ordered arrangements of atoms. In low-index crystallographic directions, atoms lie in long rows and in planes and the ordered electric fields produced by these rows and planes profoundly influence the behaviour of incident ions. If a parallel ion beam is incident along a major crystallographic axis or plane, the electric field acts to guide the ions between the rows or planes, thus preventing them from approaching individual nuclei and greatly

reducing electronic stopping and the probability of Rutherford scattering and nuclear reactions. Up to 98% of all incident ions may be trapped in axial channels by this mechanism. This phenomenon, known as channelling, has wide applications in the analysis of crystals and for semiconductor materials in particular.

**2.3. Depth scales.** In nuclear analysis spectra, it is possible to relate the energy to a depth in the sample through the energy loss relations. With the geometry shown in Figure 2, an incident ion of energy $E_0$ reacting with an atom at the surface will enter a detector placed at an angle $\psi$ to the incident beam with an energy $KE_0$, where $K$ is a proportionality constant known as the kinematic factor. If the incident ion travels a distance $x/\cos\theta_1$ into the sample before interaction, where $x$ is the depth normal to the sample surface. it will lose an energy

$$\Delta E_0 = \int_0^x \frac{x}{\cos\theta_1}\left(\frac{\mathrm{d}E}{\mathrm{d}x}\right)_{\mathrm{INC}}\mathrm{d}x, \qquad (1)$$

where $(\mathrm{d}E/\mathrm{d}x)_{\mathrm{INC}}$ is the rate of energy loss of the incident ions in the sample material. If the ion then interacts at this point it will produce a reaction product with energy $K(E_0-\Delta E_0)$. In leaving the sample on its way to the detector this particle will lose an energy

$$\Delta E_{\mathrm{PROD}} = \int_0^x \frac{x}{\cos\theta_2}\left(\frac{\mathrm{d}E}{\mathrm{d}x}\right)_{\mathrm{PROD}}\mathrm{d}x, \qquad (2)$$

where $(\mathrm{d}E/\mathrm{d}x)_{\mathrm{PROD}}$ is the rate of energy loss for the reaction product in the sample material. The energy observed at the detector will therefore be

$$E_1 = K(E_0-\Delta E_{\mathrm{INC}})-\Delta E_{\mathrm{PROD}}. \qquad (3)$$

Hence the depth scale is related to the energy scale by the difference in energy between the reaction products from the surface and from a depth $x$ and is given by

$$\Delta E_1 = (K\Delta E_{\mathrm{INC}}+\Delta E_{\mathrm{PROD}})\Delta x. \qquad (4)$$

The energy loss process relates to the sum of the interactions between ions and individual atoms in the material. It is common, therefore, to replace $(\mathrm{d}E/\mathrm{d}x)$ by a term known as the stopping cross-section $\varepsilon$ and defined as $(1/N)(\mathrm{d}E/\mathrm{d}x)$. The units of $\varepsilon$ are eV cm$^2$ per atom and usually written as eV cm$^2$. Real materials generally contain mixtures of atoms or are specific compounds. For these cases Bragg's rule is used to combine the stopping cross-sections for the individual elements in the following manner. If the compound or mixture can be represented by $A_mB_n$ and the individual stopping cross-sections are $\varepsilon^A$ and $\varepsilon^B$ then the mixture or compound has a stopping cross-section given by $\varepsilon^{AB} = m\varepsilon^A + n\varepsilon^B$. For example, for the compound $Al_2O_3$,

$$\varepsilon^{Al_2O_3} = 2\varepsilon^{Al}+3\varepsilon^{O}. \qquad (5)$$

**2.4. Nuclear reactions.** The complexity of nuclear reactions is best illustrated with the help of an energy level diagram. A typical example for deuteron bombardment of $^{16}O$ is given in Figure 3. If a deuteron of zero energy could be made to merge with an oxygen atom it would form a $^{18}F$ compound nucleus with an excitation energy of 7.515 MeV. On the potential energy diagram this is illustrated by placing the $^{16}O$ energy level diagram 7.515 MeV above that for $^{18}F$ (i.e. the $Q$ value for compound nucleus
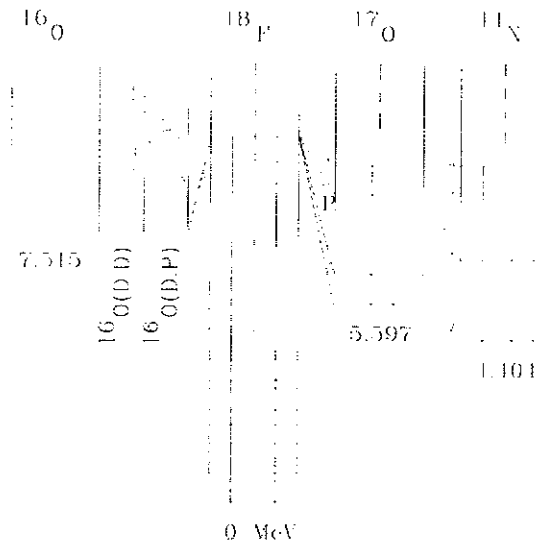
**Figure 3.** Energy levels. nuclear reactions and cross-sections for energetic deuteron reactions with $^{16}O$.

formation). This highly excited state may decay through any one of the following decay channels.

(a) A deuteron is re-emitted leaving $^{16}O$ in its ground state. This corresponds to elastic scattering and will be superimposed on the normal Coulomb scattering (Rutherford). The yield of elastically scattered deuterons as a function of incident deuteron energy is shown in the second column in Figure 3, where it can be seen that the yield follows closely the Rutherford value up to a deuteron energy of about 1.5 MeV, after which the effects of compound nucleus formation associated with various energy levels in $^{18}F$ become apparent as resonant shapes superimposed on the yield curves.

(b) The excited state of $^{18}F$ may decay by gamma emission. In this case the reaction product M2 is a gamma ray, or more probably, a cascade of gamma rays from specific excited states in $^{18}F$. In this particular example, two other particle emitting decay channels are open and as these involve strong nuclear forces, decay by these modes will usually be much more probable than by gamma decay.

(c) Another decay channel energetically open is that of alpha particle decay to $^{14}N$. The $Q$ value for alpha emission to the ground state of $^{14}N$ is 3.111 MeV. Thus the energy level diagram is placed at 4.404 MeV relative to the ground state of $^{18}F$. $^{14}N$ has excited states at 2.31, 3.95, 4.91 (below 5 MeV, there being many more above 5 MeV). Consequently, the $^{18}F$ compound nucleus found at an excitation energy of 7.515 MeV can decay by alpha emission to both the ground state and first excited state of $^{14}N$. These alpha particles are denoted as $\alpha_0$ and $\alpha_1$ respectively. As the energy of the deuteron incident on $^{16}O$ is increased, higher excitations are reached in $^{18}F$ and further alpha emission channels to higher excited states in $^{14}N$ become available.

(d) The remaining decay channel open is proton decay to the ground and excited states of $^{17}O$. Here the energy level diagram for $^{17}O$ is at 5.597 MeV and the first three excited states are at 0.871, 3.058 and 3.846 MeV. In this case, only two proton decay channels, $p_0$ and $p_1$ are immediately available. In both proton and alpha particle decay. groups decaying to excited states will
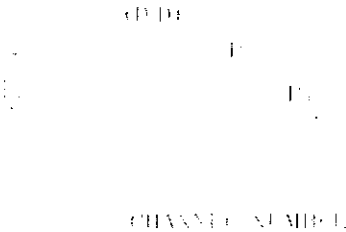
**Figure 4.** A schematic energy spectrum of the proton and alpha particle groups and elastically scattered deuterons from the bombardment of $^{16}$O with energetic deuterons. The full curves represent the response from a thin target and the dashed curves from a thick target.

give rise to gamma radiation as the states decay to the ground state. It is possible, therefore, to monitor such reactions by observing either the particles or the subsequent gamma rays. When a thin oxygen containing sample is bombarded with 1 MeV deuterons the particles and their energies observed by a changed particle detector are illustrated in Figure 4. Here two proton groups to states of $^{17}$O, two alpha groups to states of $^{14}$N and elastically scattered deuterons are observed.

**2.5. Reaction kinematics (non relativistic).** A schematic of an ion interaction with a nucleus is shown in Figure 5. Here an incident ion of mass $M_1$ and energy $E_1$ is incident upon a stationary sample atom of mass $M_2$. After the interaction, two particles are usually produced with the lighter partner having mass $M_3$ and energy $E_3$ emerging at a laboratory angle $\psi$ to the incident beam direction and a heavier partner $M_4$ emerging at a laboratory angle $\xi$ with an energy $E_4$. Such an interaction $M_1 + M_2 \rightarrow M_3 + M_4 + Q$ is usually written as $M_2(M_1, M_3)M_4$, $Q$ where $Q = (M_1 + M_2 - M_3 - M_4)c^2$ and can be positive, negative, or zero, depending on the type of interaction. Also, the total energy of the system

$$E_T = E_1 + Q = E_3 + E_4. \tag{6}$$

Standard kinematic calculations then give

$$\frac{E_3}{E_1} = B[\cos \psi \pm (D/B - \sin^2 \psi)^{1/2}]^2. \tag{7}$$

where the positive sign should always be used, except when $B > D$ in which case $\psi_{max} = \sin^{-1}(D/B)^{1/2}$. Also,

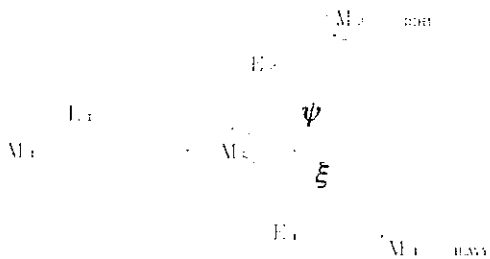$$\frac{E_4}{E_1} = A[\cos \xi \pm (C/A - \sin^2 \xi)^{1/2}]^2. \tag{8}$$



**Figure 5.** A schematic representation of the interaction of an energetic ion $M_1$ with a sample nucleus $M_2$, giving rise to a light reaction product $M_3$ and heavy reaction production $M_4$.

Again only the positive sign is used unless $A > C$ in which case $\xi_{max} = \sin^{-1}(C/A)^{1/2}$.

$$A = \frac{M_1 M_4 (E_1/E_T)}{(M_1 + M_2)(M_3 + M_4)}.$$

$$B = \frac{M_1 M_3 (E_1/E_1)}{(M_1 + M_2)(M_3 + M_4)}.$$

$$C = \frac{M_2 M_3}{(M_1 + M_2)(M_3 + M_4)}\left[1 + \frac{M_1 Q}{M_2 E_1}\right] \quad \text{and}$$

$$D = \frac{M_2 M_4}{(M_1 + M_2)(M_3 + M_4)}\left[1 + \frac{M_1 Q}{M_2 E_T}\right].$$

It should be noted that $A + B + C + D = 1$ and $AC = BD$. A special case of the above formulae is for elastic scattering, when $M_1 = M_3$, $M_2 = M_4$ and $Q = 0$.

**2.6. Scattering cross-section $d\sigma/d\Omega$.** When energetic ion beams are used in materials analysis, reaction products are observed at an angle $\psi$ to the incident beam using a detector which subtends a small solid angle (typically $< 10^{-3}$ str). The count rate in the detector from a thin sample is given by

$$Y = INx\frac{d\sigma}{d\Omega}\Omega\varepsilon. \tag{9}$$

Where $I$ is the incident beam current expressed as the number of incident ions per second, $N$ is the number of atoms per unit volume in the sample undergoing the observed interaction, $x$ is the sample thickness. $d\sigma/d\Omega$ is the differential scattering cross-section for the reaction into an element of solid angle at the observation angle $\psi$, $\Omega$ is the detector solid angle and $\varepsilon$ is the detector efficiency. In general, $d\sigma/d\Omega$ is quoted for a given incident energy and detection angle and a small element of solid angle. If thick targets are to be analysed or large solid angle detectors are used then the above equation must be integrated over the detector solid angle and the energy of the ions as they penetrate the sample.

For Rutherford elastic scattering the cross-section has a well defined analytical form given by the Rutherford formula

$$\frac{d\sigma}{d\Omega} = \left[\frac{Z_1 Z_2 e^2}{16\pi\varepsilon_0 E_1}\right]^2 \frac{4}{\sin^4 \psi}$$

$$\times \frac{[[1 - ((M_1/M_2)\sin \psi)^2]^{1/2} + \cos \psi]^2}{[1 - ((M_1/M_2)\sin \psi)^2]^{1/2}}. \tag{10}$$

In many applications of Rutherford backscattering analysis $M_1 \ll M_2$. In this case, the Rutherford formula simplifies to

$$\frac{d\sigma}{d\Omega} = \left[\frac{Z_1 Z_2 e^2}{16\pi\varepsilon_0 E_1}\right]^2 \text{cosec}^4 \frac{\psi}{2}. \tag{11}$$

Unfortunately, there is no such simple analytical form for nuclear reaction cross-sections. Here the value of the cross-section depends, in a very complex way, on the particles involved, the incident ion energy and the nuclear physics of the excited compound nucleus. In general, however, the magnitude of the cross-section is heavily influenced by the Coulomb barrier; the Coulomb repulsion which prevents an ion and nucleus coming close

enough together for nuclear reactions to occur. The Coulomb barrier has a value proportional to

$$\frac{Z_1 Z_2}{(A_1^{1/3} + A_2^{1/3})} \frac{M_1 + M_2}{M_2},\qquad(12)$$

where $A_1$ and $A_2$ are the atomic mass number of the ion and struck atom respectively. Very roughly, the Coulomb barrier for proton or deuteron beams is $\geqslant 2.5$ MeV for elements with atomic number $\geqslant 10$ and atomic number $\geqslant 5$ for alpha particle beams. Cross-sections tend to be higher near the Coulomb barrier for loosely bound incident ions such as deuterons and $^3$He. For beams of a few MeV, nuclear reactions with reasonably large cross-sections are limited to combinations of light incident ions and elements with atomic number less than about 20. For some nuclear reactions with light elements, the excited states of the compound nucleus are well spaced in energy and have a very narrow energy width. In such cases, cross-sections often only exist at incident ion energies which correspond to excited states. These are known as resonance cross-sections.

## 3. Analysis techniques

### 3.1. Transmission ion microscopy.
The simplest analytical measurement that can be made is to measure the energy loss of ions in passing through thin samples of material. The electronic stopping process has a rate of energy loss $(dE/dx)_e$ $\alpha(NZ_1^2 Z_2/E_1)$. Hence, for a thickness of sample $x$, the loss in energy $\Delta E$ varies as $NZ_2 x$. By measuring energy loss as a function of position, by scanning an ion beam uniformly over a sample or by moving the sample under the beam, it is possible to build up a topographical map of the relative stopping power of the sample. The technique is very powerful because in principle, a measurement can be made at each location with a single ion. In practice, however, the energy loss of several ions is averaged at each point on the map. Information can be quickly collected with an extremely small beam current of only a few thousand ions per second, thus greatly reducing the possibility of damage to the sample or loss of volatile material. The technique, known as Scanning Transmission Ion Microscopy (STIM) is ideal for use with extremely small beam spots of less than one micron diameter when very high spacial resolution images are obtainable. The range of 3 MeV protons in most materials is of the order of 50 $\mu$m and samples of several tens of microns thickness can easily be measured. Alpha particles of the same energy have a range around 10 $\mu$m and are commonly used for samples of a few microns thickness. Heavier ions can be used with even thinner samples.

STIM measurements generally have two types of application. As ion beam analysis measures the number of atoms in the path of the beam, it is not possible to convert this measurement into an elemental concentration unless the thickness of the sample is known. Hence, if for example, elemental concentrations in an unsectioned biological sample are to be determined, the elemental yields must be correlated with the thickness at each point. Assuming that the elements of interest are minor or trace elements, the $NZ_2$ term will be determined by the biological matrix and the energy loss values measured by STIM will provide a direct measure of the thickness. Elemental yields and STIM thickness therefore allow concentrations to be determined. Another example of the application of STIM is where a sample has a uniform thickness but contains regions of different elemen-
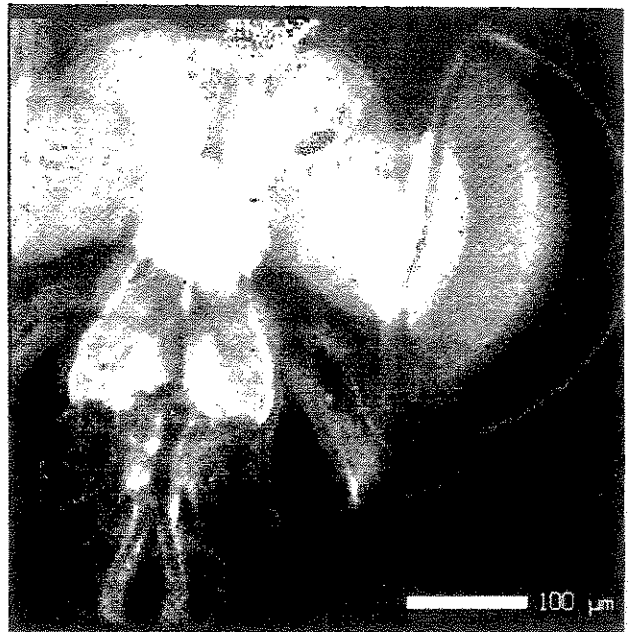


**Figure 6.** A 4 MeV H⁻ STIM image of part of the head of a fruit fly. Whiter areas indicate larger proton energy loss. The highest energy loss corresponds to about 0.1 kg m⁻². (Reproduced by permission of H W Lefevre *et al*, ref 12.)

tal composition. An example of this type of sample is an electronic micro circuit which may be made up of layers of silicon, oxides or nitrides and perhaps heavy metal connecting strips. Here STIM is able to image the contrasting $NZ_2$ components and can clearly image buried metal strips invisible from the surface. An excellent review and bibliography of the STIM technique has been published by Lefevre *et al*[12].

Figure 6 shows a STIM image measured by Schofield *et al*[13], 4 MeV protons were used to bombard the freeze dried head of a fruit fly and the energy of the penetrating protons were measured in a surface barrier detector placed 1 cm behind the object. The image is composed of $256 \times 256$ pixels, the whiter areas corresponding to larger proton energy loss. The maximum energy loss indicates an areal density of 0.1 kg m⁻². The mouthparts of the head are at the bottom and the eye occupies the upper right of the picture. In a subsequent analysis of the Ca content of the head using X-ray emissions, an uncorrected image of the Ca distribution was obtained. This image was then divided pixel by pixel by the STIM areal density image to provide a Ca concentration distribution, as shown in Figure 7. Here it can be seen that the highest Ca concentration appears in the retinular cell region of the compound eye.

### 3.2. Rutherford backscattering.
Rutherford backscattering (RBS) is probably the most widely used and easiest understood of the ion beam analysis techniques. Elastically scattered ions behave as billiard balls in bouncing from nuclei in the sample and the energy and yield of the scattered ions can be measured with a suitable particle detector. Elastic scattering is a special case of the kinematics equation (7) where $M_1 = M_3$, $M_2 = M_4$, $Q = 0$ and $E_1 = E_T$. In RBS experiments $M_2$ is usually greater

## CALCIUM X-RAYS    AREAL DENSITY    Ca X-RAYS/AREAL DENSITY
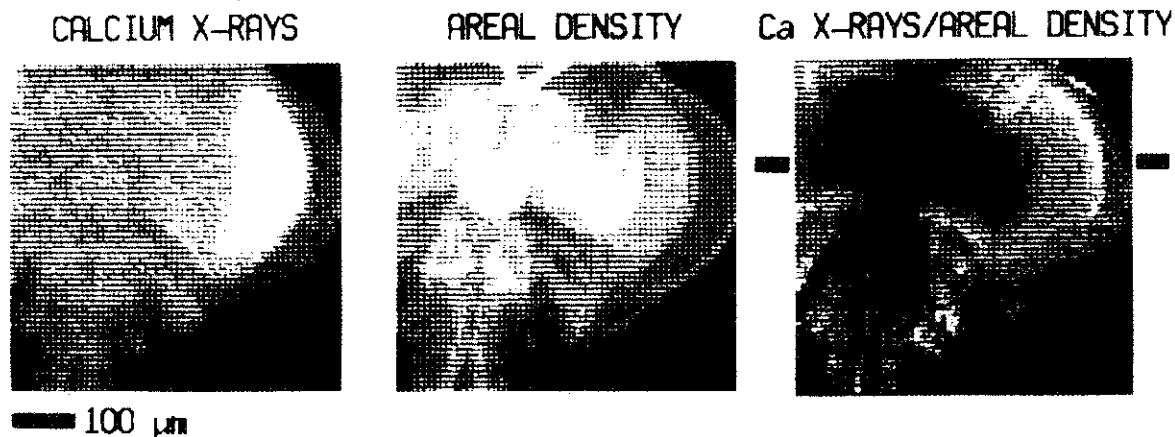


**100 μm**

**Figure 7.** Images of the head of a fruit fly formed by Ca X-rays, STIM energy loss and the pixel by pixel ratio of the X-ray image to the aerial density. Whiter areas indicate areas of higher X-ray yield, areal density and concentration. (Reproduced by permission of H W Lefevre *et al*, ref 12.)

than $M_1$ and the kinematic factor reduces to

$$K = \left[ \frac{M_1 \cos\psi + (M_2^2 - M_1^2 \sin^2\psi)^{1/2}}{M_1 + M_2} \right]^2 . \tag{13}$$

Here $K$ depends only on $M_1$, $M_2$ and $\psi$. Hence a measurement of the energy of the elastically scattered ions at a particular angle $\psi$ allows the determination of $M_2$. The value of $K$ varies with $\psi$ and has its smallest rate of change near $\psi = 180$. Also, the difference in energy between different $M_2$ values is a maximum at $\psi = 180$ for all but the lighter values of $M_2$. Thus in most RBS measurements, scattered particles are detected at values of $\psi$ as close to 180 as is reasonably achievable. Here the energy spread introduced by the finite angle of the detector is a minimum and the ability to distinguish sample atoms of different mass is the greatest. The energy separation of 2 MeV $^4$He, $^{16}$O and $^{35}$Cl ions, backscattered from atoms of consecutive mass, is shown in Figure 8. Note that the energy separation for the heavier sample atoms increases as the incident ion mass increases and also increases linearly with the ion energy. If the scattered particle energies could be measured with absolute accuracy, atoms of consecutive mass at the surface of a sample could be resolved for all masses. In real life, however, the energy resolution of the detector system must be taken into account. Conventional silicon surface barrier detectors have an energy resolution of about 15 keV for alpha particles. Thus, when using 2 MeV He ions, the maximum sample atom mass at which consecutive masses can be resolved is about 45. In principle, the limit can be pushed higher by using heavier ions. However, these produce much higher ionization densities, with an increased probability of recombination and a larger fraction of their energy loss is through non-ionizing nuclear stopping processes. This results in a resolution in silicon detectors as high as 100 keV for oxygen ions and even higher for heavier ions. Some of this disadvantage can be compensated for by using higher energies, although ion beam damage in the sample then becomes a greater problem.

A typical RBS response for 2 MeV alpha particles scattered at 175, for a sample composed of a uniform mixture of equal parts by weight of silver silicon and carbon, is shown in Figure 9. Figure 9(a) shows the spectrum from a thin sample, Figure 9(b) from an intermediate sample and Figure 9(c) from a sample thick enough to stop the alpha particles. The rounding of the edges of

the three groups is dominated by the detector resolution which, in this case, was 15 keV. It can be seen from the scattering cross-section, equation (11), that for a given ion and detection angle $\sigma \propto (Z_2^2/E_1^2)$. Hence RBS is very sensitive to high $Z_2$ elements and insensitive to low $Z_2$ elements. The generally rising yield towards lower energies in the thick target spectrum reflects the $E_1^{-2}$ dependence of the cross-section. The technique is most suited to the determination of heavy elements, particularly if they are in a light element matrix. Also, because of the analytical value of the cross-section, when the system geometry and integrated beam charge are known, the areal density of the sample ($Nx$) can be measured absolutely without resort to the use of standards. Elemental depth profiles can also be determined without destroying the sample. For relatively thin samples, when the stopping cross-section through the thickness of the sample can be taken as constant, equation (3) can be used to define a depth scale parameter $\varepsilon'$

$$\varepsilon' = \frac{K\varepsilon_{INC}}{\cos\theta_1} + \frac{\varepsilon_{PROD}}{\cos\theta_2} . \tag{14}$$
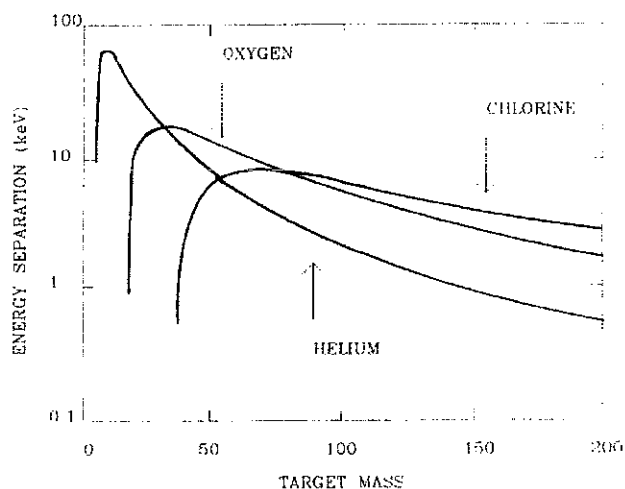


**Figure 8.** The energy separation of 2 MeV $^4$He, $^{16}$O and $^{35}$Cl ions, backscattered at an angle of 180 from atoms of consecutive mass.
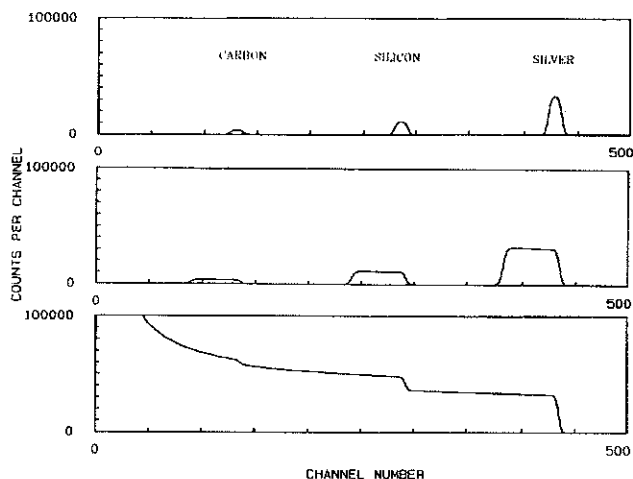
**Figure 9.** A typical RBS response for 2 MeV alpha particles scattered at 175° from a sample composed of a uniform mixture of equal parts by weight of Ag, Si and C. Part (a) is for a thin sample; (b) for a semi-thick sample; and (c) for a sample thick enough to stop the alpha particles.

The spectrum for such samples can be analysed very easily. The distributions shown in Figure 9(b) have a width inversely proportional to $\varepsilon'$ and a total area proportional to $Z_2^2$. The step height of the distributions is therefore proportional to $Z_2^2/\varepsilon'$. If the layer to be measured is sufficiently thin that the contribution from different elements do not overlap, then the stoichiometry of the layer can be accurately measured directly from the ratio of the square of the atomic numbers and the yields in the peaks. If, however, the contributions overlap significantly then the step height from each element must be used and the stopping cross-section must also be known. Stopping cross-sections have been tabulated[14] and are accurate to better than 5% for helium ions.

Typical spectra for RBS analysis of a thin $YBa_2Cu_3O_7$ superconductor film on a MgO backing are shown in Figure 10. At an alpha particle beam energy of 1 MeV, shown in Figure 10(a), the energy loss in the film is sufficient to cause the groups to overlap.
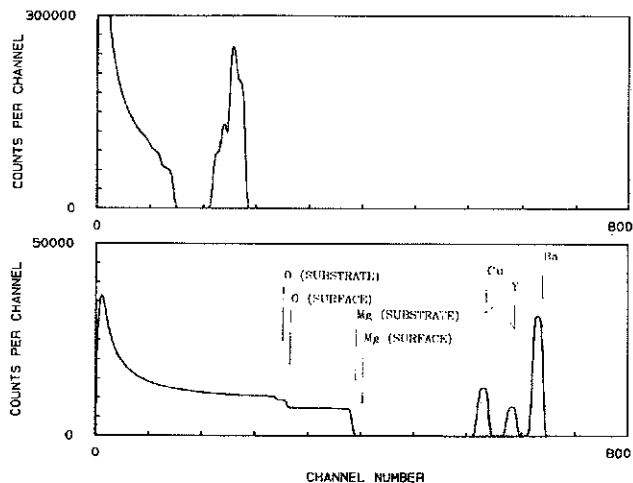


**Figure 10.** Typical alpha particle RBS spectra from a thin layer of $YBa_2Cu_3O_7$ superconductor on a MgO substrate; (a) 1 MeV beam showing overlap of signals from the different elements; (b) 3 MeV beam showing separation of the individual contributions.

At the higher energy the stopping cross-sections are less and the contributions from individual metals are clearly separated. The insensitivity to light elements is evident in these spectra, making the accurate determination of oxygen very difficult. Note that the leading edge of the Mg signal has been displaced downward in energy by the energy loss in the superconductor layer. This illustrates the ambiguity of RBS spectra where, for complex spectra, it is not always easy to differentiate between the signal from an element on the surface and a heavier element at a point beneath the surface.

One of the biggest advantages of RBS is the analytical form of the Rutherford cross-section, which enables absolute elemental concentrations to be determined. Great care is usually taken, therefore, to use only ions and energies for which this relationship holds. In such cases, the depth of analysis possible is usually restricted to the order of one micron. Once departures from Rutherford occur, experimentally determined cross-sections must be employed in analysing spectra and accuracy is reduced as cross-section data are not always well known. However, considerable advantages can be gained for certain elements if ion energies are chosen carefully. For example, the $^{16}O$ $(\alpha,\alpha)^{16}O$ cross-section has a large sharp resonance at 3.06 MeV at backward angles where the peak cross-section is nearly thirty times higher than Rutherford. At still higher energies, the cross-section is greatly enhanced by a number of resonances, as is shown in Figure 11. Between 7 and 8 MeV alpha energy there is a region of reasonably constant cross-section which is enhanced above Rutherford by a factor greater than $10^5$. This is an ideal energy range for measuring oxygen concentrations in a heavy element matrix where conventional RBS would be totally ineffective.

### 3.3. Elastic recoil detection analysis (ERDA).

When $M \geqslant M_2$, ions cannot backscatter. However, useful information can be gained about the $M_2$ atoms by measuring their forward recoil energies. From equation (8) the recoil energy is

$$E_3 = E_1 \frac{4M_1 M_2}{(M_1 + M_2)^2} \cos^2 \zeta = K' E_1. \tag{15}$$

Maximum energy is transferred when $M_1 = M_2$ and $\zeta = 0°$. The technique relies on being able to discriminate between the scattered incident ions and the forward recoil nuclei. The most common application makes use of energetic helium ions to measure the isotopes of hydrogen, an element of great technological importance and one which is notoriously difficult to measure. The sample is placed at a glancing angle to the incident beam of $\theta = 15°$ and $\zeta$ is usually restricted to 30° to maximise $E_4$ (Figure 12).
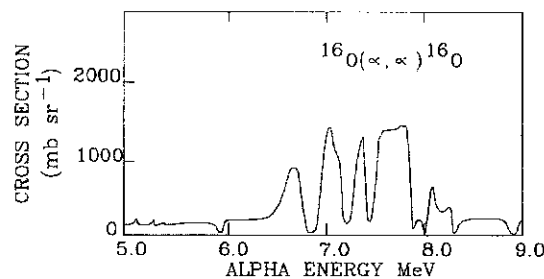


**Figure 11.** The alpha particle elastic scattering cross-section from $^{16}O$ at an angle of 170° between the incident energies of 5 and 9 MeV.

**Figure 12.** A schematic representation of a typical arrangement for ERDA analysis.

As helium has a higher stopping power than hydrogen, it is possible to exclude the scattered beam from the detector by covering it with foil which is just thick enough to stop the beam particles but which will transmit the hydrogen isotopes. For 3 MeV He ions, surface deuterons recoil at around 2 MeV and hydrogen at around 1.5 MeV and lose about 300–400 keV respectively in passing through a detector foil just thick enough to stop the scattered alphas. Because of the shallow angle, depth scales, which are generated in the same manner as with RBS spectra, are limited to a few hundred nm. Energy resolution is very sensitive to surface topography because of the shallow angles involved and to the accurate positioning of the sample in the beam. Kinematic energy spread is given, from equation (15), by

$$\Delta E_3 = E_1 \frac{4 M_1 M_2}{(M_1 + M_2)^2} \sin 2 \xi \, d\xi. \tag{16}$$

For the example quoted above this has a value of 28 keV for an angular spread $d\xi = 1$. Energy straggling in the detector foil has a comparable value, giving an overall spread, assuming 15 keV detector resolution, of the order of 40 keV and a resulting surface depth resolution of about 20 nm. The technique typically has a bulk sensitivity of about 0.1 at% and is sensitive to 0.1 monolayers on a surface. Usually, absolute concentrations are determined by reference to standards. Typical 3 MeV He⁺ ERDA spectra are shown in Figure 13 for a 96 nm plasma deposited $Si_3N_4$ layer on a Si substrate before and after a high temperature anneal. The as-produced sample contains 28% atoms of hydrogen whilst in the annealed sample the hydrogen concentration is reduced to 7% atoms. The small number of counts below the main peak are probably due to multiple scattering in the sample and detector absorber foil.

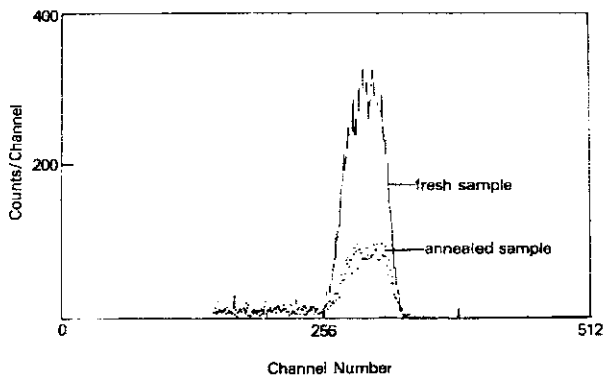A variation on the above technique is to use a sample which

is thin enough to just stop the incident He beam, in which case the foil can be placed normal to the beam and hydrogen isotopes can be detected at 0. A further variation of the thin foil approach is to bombard with protons and to observe both the recoil hydrogen atom and the scattered proton in coincidence in detectors placed at ±45 to the beam. Here the sum of the energy in the two detectors is found to increase with the distance travelled through the foil by the incident proton before scattering and a depth profile is obtained from the summed energy spectrum. The coincidence requirement greatly reduces background and detection sensitivities as low as 1 ppm atoms have been achieved.

In some of the major facilities, usually ex-nuclear structure research machines, ions of oxygen, sulphur and chlorine can be accelerated to several tens of MeV and use of these ions in the ERDA geometry enables elements from hydrogen to around oxygen (with ³⁵Cl ions) to be measured. The problem experienced here is in distinguishing the various recoil ions. Even though the heavier ions have the highest recoil energies, they also have the highest stopping cross-sections and consequently often appear at lower energies in the final spectrum. In such cases, it is a great help to have a good idea of the elements to be expected in the sample. Figure 14 shows an example of an ERDA spectrum taken from a CVD-deposited film of diamond-like carbon, using 30 MeV ³⁵Cl ions. The high energy peak is from recoil carbon and corresponds to a thickness of 91 nm (assuming a density of 2270 kg m⁻¹). Oxygen, which initially has a higher recoil energy but also has a higher stopping power, is present as the intermediate distribution and the low energy peak is from hydrogen. Both oxygen and hydrogen are found to be distributed throughout the foil, the narrowness of the hydrogen peak reflecting the much lower stopping power of hydrogen. The respective concentrations are found to be 74% atoms of carbon, 3% atoms of oxygen and 23% atoms of hydrogen. The accuracy is typically better than 5%.

**3.4. Nuclear reactional analysis (NRA)—non-resonant.** Non-resonant nuclear reaction and Rutherford backscattering analysis have many features in common. Both techniques measure the energy distribution of reaction products or scattered ions and determine elemental concentrations and depth profiles from the yields and ion energy loss relations, as illustrated in Figure 2. With NRA, however, reaction cross-sections have no easily pre-
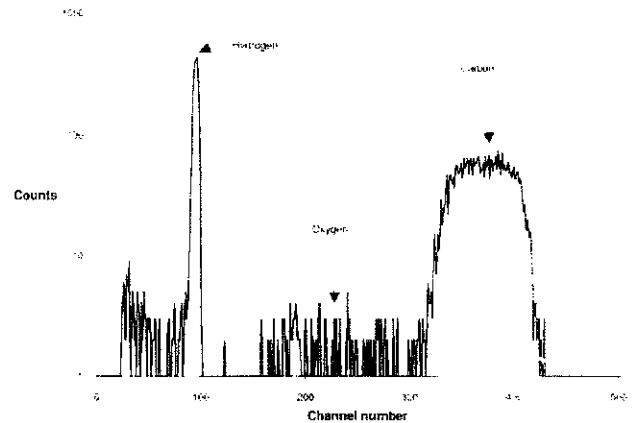


**Figure 13.** Proton recoil spectra, measured at 30, from the 3 MeV He⁺ bombardment of a 96 nm plasma deposited $Si_3N_4$ layer on Si, before and after annealing.



**Figure 14.** Elastic recoil spectrum of a 91 nm diamond-like carbon coating on Si, recorded using 30 MeV Cl ions (reproduced by permission of AEA Technology, copyright © UKAEA 1992).
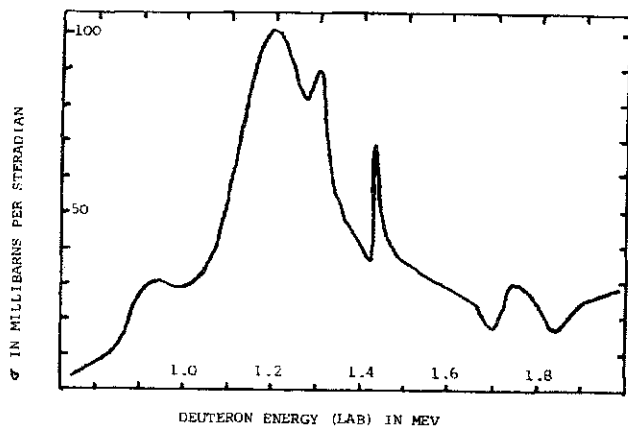
**Figure 15.** The laboratory differential cross-section for the $^{12}C(d, p_0)^{13}C$ reaction at a laboratory angle of 135°.

dictable value or variation with ion energy. Interpretation of the energy spectra must therefore rely on experimentally measured cross-sections, with a consequent reduction in accuracy, or on comparisons with spectra from standard materials. The differential cross-section for the $^{12}C(d,p)^{13}C$ reaction at a laboratory angle of 135° is shown as a function of incident deuteron energy in Figure 15 and the proton energy spectra from the 1.5 and 2.0 MeV deuteron bombardment of a thick graphite sample, as shown in Figure 16. The link between the proton yield as a function of deuteron energy as the beam slows down in the graphite and the reaction cross-section is clearly visible. The analysis depth for 1.5 and 2.0 MeV deuterons in graphite is 8 $\mu$m and 17 $\mu$m respectively. Nuclear cross-sections are strongly influenced by the Coulomb barrier and generally only have usefully high values for elements with $Z_2 < 16$. NRA is consequently excellent for measuring the distribution of low $Z_2$ elements, especially when contained in a high $Z_2$ matrix, and therefore complements RBS analyses very well. Most isotopes from $^1H$ to $^{32}S$ can be determined with good sensitivity for the lighter elements, which are often difficult to measure by other techniques. Unlike RBS, which produces thick sample spectra extending down to zero scattered ion energy, nuclear reaction products usually cover a finite energy range. This is because reactions are usually chosen to have a positive $Q$ value which imparts a finite energy to the reaction products, even when the incident ion energy approaches zero.

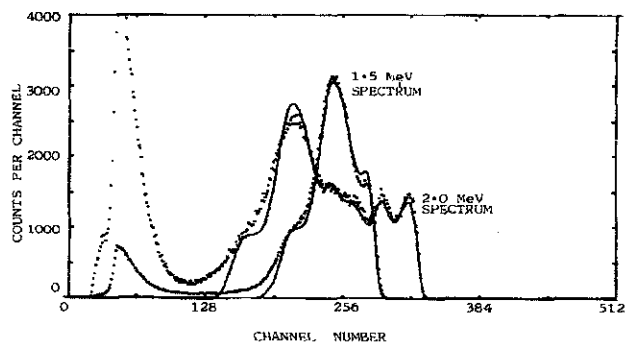Nuclear reaction spectra are usually highly complex, depend-

ing upon the nuclear properties of both the incident ion and the sample nucleus, the incident ion energy, reaction $Q$ value, excited states of both the compound nucleus and daughter nucleus, the reaction cross-section and the angular distribution of the reaction products. However, the spectrum or reaction product 'signature' is unique and highly specific to each isotope. This makes NRA an excellent technique for studying chemical reaction dynamics because the behaviour of different isotopes can be easily distinguished. For example, the pairs of isotopes $^{12}C/^{13}C$, $^{14}N/^{15}N$ and $^{16}O/^{18}O$ all have quite different 'signatures'. Nuclear reaction cross-sections tend to become smaller and excited states closer together for higher $Z_2$ nuclei, giving rise to very complex spectra. In general, therefore, only two or three isotopes can be measured simultaneously. Care must also be exercised in choosing the appropriate beam ion, energy and detection angle to ensure optimum separation of the signals from different isotopes. A typical NRA particle spectrum, obtained from the 1.1 MeV deuteron bombardment of a thin titanium nitride sample, is shown in Figure 17. Most of the observed peaks are from the $^{14}N(d,p)^{15}N$ reaction although peaks from $^{14}N(d,\alpha)^{12}C$ and $^{12}C(d,p)^{13}C$ are also visible. Carbon is present as a surface contaminant.

The most commonly used nuclear reactions are carried out with proton, deuteron or $^3He$ ion beams. With proton beams the usual method is to measure gamma rays from inelastic scattering, capture or $(p,\alpha\gamma)$ reactions. The majority of NRA measurements detect charged particle reaction products however, making use of the high positive $Q$ values for reactions induced by the loosely bound D and $^3He$ ions. In these cases it is usual to place a foil over the detector, thick enough to prevent elastically scattered ions being detected but thin enough to allow reaction products to pass through into the detector. Nuclear reaction cross-sections are usually very much smaller than those for elastic scattering and the removal of the high fluence of scattered ions enables higher beam currents to be used to improve count rates. In many laboratories deuteron induced reactions are favoured. However, large numbers of fast neutrons are also produced by $(d,n)$ reactions, in beam line components as well as in samples, and due attention must be paid to the provision of adequate neutron shielding when employing deuteron beams. NRA sensitivities vary greatly with the reaction and usually lie in the range of % down to mg g$^{-1}$. If a moveable detector foil is employed, it is



**Figure 16.** Spectra of protons measured at 135° from the 1.5 MeV and 2.0 MeV deuteron bombardment of a thick sample of pure carbon. The smooth curves show the simulated spectra.
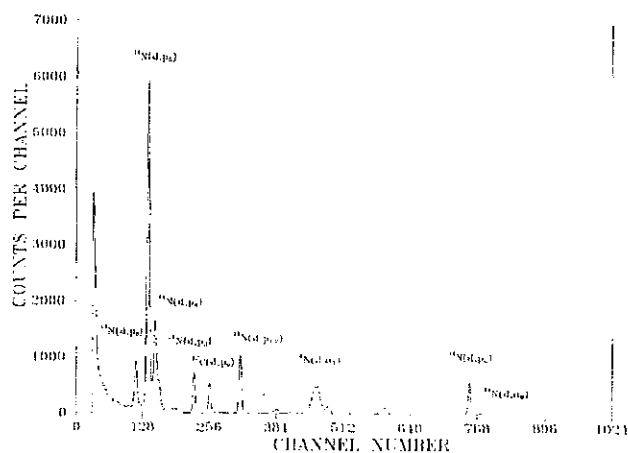


**Figure 17.** A typical NRA spectrum from the 1.1 MeV deuteron bombardment of a thin TiN sample.

possible to measure both NRA and RBS spectra, thus determining the detector solid angle calibration by using the RBS data.

**3.5. Nuclear reaction analysis—resonant reactions.** With the non-resonant reactions described in the previous section, the reaction cross-section varies with the incident ion energy and is generally a continuous function. However, some reactions, known as resonant nuclear reactions, exhibit very large increases in cross-section at well defined energies corresponding to specific excited states of the compound nucleus. Such resonances have a full-width-at-half-maximum which is a property of the excited state and which may have values ranging from electron volts or less up to many thousands of electron volts. An excellent example of a resonant cross-section is provided by $^{19}F(p, \alpha\gamma)^{16}O$ and is shown in Figure 18 for proton energies from 0.5 to 1.5 MeV.

The analysis of materials using resonant nuclear reactions requires a different approach. If an ion beam of a given energy bombards a sample containing an element with a resonant cross-section, the reaction will only occur for very thin layers in the sample at which the ion energy is at the resonance energy. As the incident ion energy is increased above the resonance energy, the reaction will occur at a greater depth in the sample. This effect is illustrated in Figure 19 for the case of an element distributed in a thin layer on the surface, with a second thin layer buried in the sample, and where the yield is plotted against the difference between the incident ion energy and the resonance energy. This difference, being the energy loss by the beam in arriving at the resonance energy, is easily converted to a depth using the usual energy loss relations. The square distributions in Figure 19 represent an idealised case where the flat tops reflect the fact that, if the resonance energy is entirely within the region containing the element of interest, the yield has a constant maximum value. This ideal response is modified at the surface by the energy spread in the beam and the energy width of the resonance and beneath the surface by the additional broadening effects of energy straggling. It should be noted that for resonance analysis the depth information is determined only by the incident ions and not the reaction products. In favourable cases, nuclear resonance analysis can achieve a depth resolution of 1 nm at the surface and can profile elemental concentrations to a depth of 10 $\mu$m. Sensitivities depend on the reaction cross-section and the presence of interfering radiation and typically range from % down to 1 ppm atoms. The depth to which elements can be profiled is often
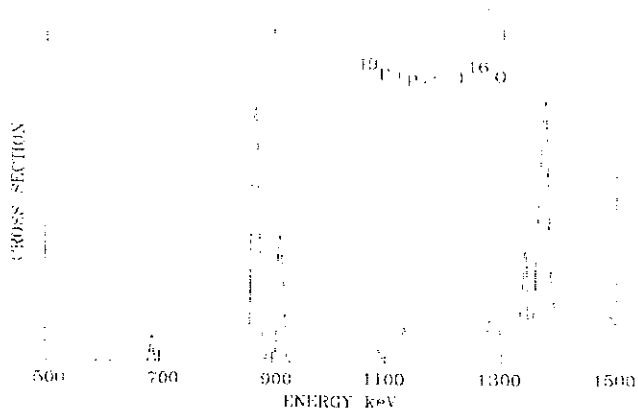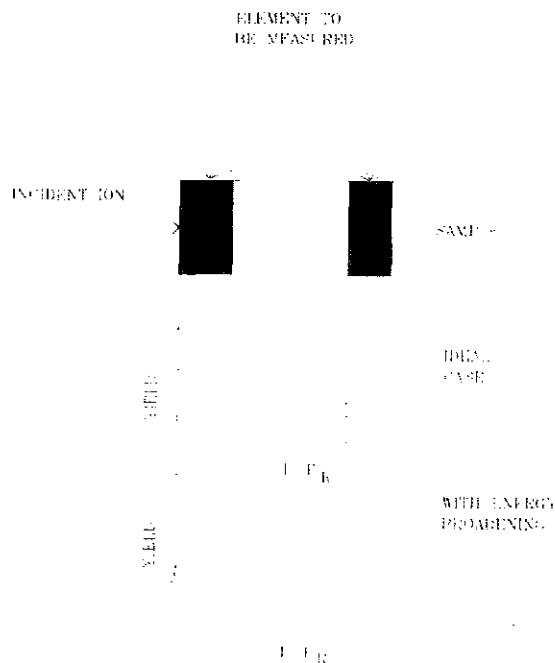


**Figure 19.** A schematic representation of resonance reaction depth profiling showing reaction yield as a function of beam energy above the resonance energy $(E - E_R)$ for a surface and buried layer. The rounded yield curves show the effect of beam energy spread, resonance width and energy straggling.

limited by the presence of additional resonances which greatly complicate the response. As with non-resonant nuclear reaction analysis, uncertainty in the nuclear resonance parameters often limit the accuracy of concentration determinations and measurements are usually made by comparison with the response from a known sample with a similar material matrix. In addition, accurate stopping power data is required when assigning depth scales. This is no problem when trace levels in a fixed matrix are being measured, but is sometimes difficult to determine when the element of interest is a major constituent which may be varying rapidly as near an interface. A major advantage of resonance analysis is that the ion beam energy can be set just above resonance energy, thus sampling the concentration below the surface and consequently free from the influence of surface contamination. The technique is much slower than RBS or non-resonant NRA because measurements must be made at many different beam energies. A comprehensive list of resonances used in depth profiling has been provided in table 14.13 of ref 9.

As many of the resonant reactions are induced by protons, a useful application is to use the reverse reaction to study hydrogen distributions. For these reactions, the centre-of-mass motion is very high. Hence, for example, the resonances at 0.340 MeV and 0.872 MeV for $^{19}F(p, \alpha\gamma)^{16}O$ are at 6.418 MeV and 16.568 MeV for the reverse $^1H(^{19}F, \alpha\gamma)^{16}O$ reaction. The technique is only possible therefore in laboratories possessing a high energy accelerator.

**3.6. Data analysis.** When RBS measurements are made in the regions where cross-sections are Rutherford, analysis of spectra is often not too difficult. However, in cases where nuclear enhanced cross-sections are used or elemental concentration profiles are changing rapidly with depth, the analysis of spectra is much more



**Figure 18.** The differential cross section for the $^{19}F(p, \alpha\gamma)^{16}O$ resonant reaction between the energies of 0.5 and 1.5 MeV.

difficult. Similarly, NRA spectra are always complex and simple interpretation and analysis is rarely possible.

The most common approach to analysis is to use computer codes to simulate measured spectra and through these to infer elemental distributions. It is rare that the constituent elements of a sample to be analysed are totally unknown. The simulation technique, therefore, consists of making an educated guess at the composition and structure of a sample (often also from the appearance of the spectrum) and calculating the resulting RBS or NRA spectrum. This is then compared with the measured data and adjustments made to the input structure until the simulated and experimental spectra agree (using a least squares criterion). Particular attention is paid to the fits to step heights and to leading edge positions, as energy shifts can indicate the presence of surface layers (oxides or contaminants for example). If a matrix contains significant levels of light elements such as carbon, nitrogen or oxygen which are not well determined by RBS, it is often advisable to perform both RBS and NRA analysis as accurate determinations require a good knowledge of all the elements present for inclusion in the stopping power calculation. The computer code contains tabulated stopping power data for all elements and either calculates Rutherford cross-sections for RBS or uses tabulated values for non-Rutherford or reaction cross-sections. The effects of straggling in the sample and detector absorber foil (if used) are included in the calculations, as is the energy resolution of the detector system. In more sophisticated programs, natural isotopic abundances are included for RBS and the energy spread caused by the finite detector angle can also be included. Figure 16 shows measured and simulated proton energy spectra from the deuteron bombardment of a thick pure graphite sample. Good fits are obtained to the data except for the lowest energy regions of the 2 MeV spectrum, which corresponds to a depth in excess of 20 $\mu$m and probably suffers from the effects of multiple scattering events.

**3.7. Channelling.** Since the late 1960s ion implantation has been used almost exclusively in selectively doping semiconductors. The advantage of ion implantation is the accurate control it affords of the dose and location of the dopant. However, the resulting damage introduced by the ion beam must be satisfactorily annealed out. Channelling has been developed largely to provide a simple method of monitoring damage removal and of studying the atom location in the lattice of the implanted dopants. It also has wide application in the analysis of other crystalline materials, such as the recently developed thin film high-$T_c$ superconductors and the range of thin films manufactured by epitaxial growth on crystalline substrates.

The principle of channelling can be illustrated by Figure 20. When a parallel beam of ions is incident along a major crystallographic axis or plane, the average field of the columns or planes of atoms act to gently guide the ions down the centre of the channel. The ions spiral down the axis, with a characteristic wavelength of a few tens of nm, in a region where the electron density is at its lowest. The rate of energy loss is therefore less for channelled ions and the ions never come close enough to the lattice nuclei to suffer RBS. A small fraction of the incident ions will collide with nuclei in the top plane of atoms and be scattered. However, subsequent crystal atoms will be in the shadow of the top atom and cannot contribute to the RBS yield. For helium ions channelled down a major crystallographic axis, the RBS yield from atoms behind the first layer can be as low as 1% of that
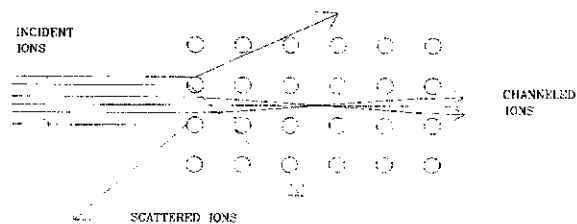


**Figure 20.** A schematic representation of the possible paths of particles in a parallel beam of ions incident along a crystal axis or plane.

from an amorphous sample of the same material. If the ion beam is gradually directed away from the crystal axis, an angle will be reached, known as the critical angle $\psi_c$, at which the steering effect can no longer channel the beam and the RBS yield will increase. Initially the yield rises above the amorphous sample level but within a degree or so reaches the equivalent amorphous or 'random' sample level. Such an angular yield curve is illustrated in Figure 21. For helium ions, the width of the angular yield curve $\psi_{1/2}$ lies typically within the range $\psi_{1/2} = 0.3-1.2^\circ$. More generally, $\psi_{1/2}$ varies as $[Z_1Z_2/Ed]^{1/2}$, where $E$ is the incident ion energy and $d$ is the distance between the lattice atoms in the direction of the beam. RBS spectra, measured for both random and aligned crystals are illustrated in Figure 22. The ratio of the minimum yield just below the surface peak and the random yield is known as $\chi_{min}$. For channelling of He ions down a major axis $\chi_{min}$ can be as low as 0.01.

One of the most straightforward channelling applications is the location of impurities or implanted dopant atoms in a crystal
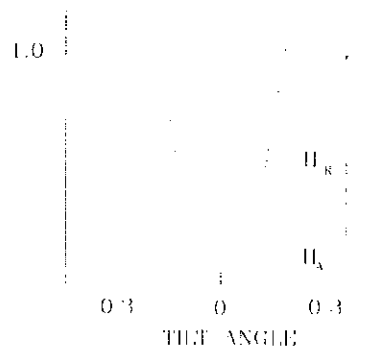


**Figure 21.** A plot of the ratio of the channelled to random RBS yield as a crystal is tilted relative to a channelling axis.
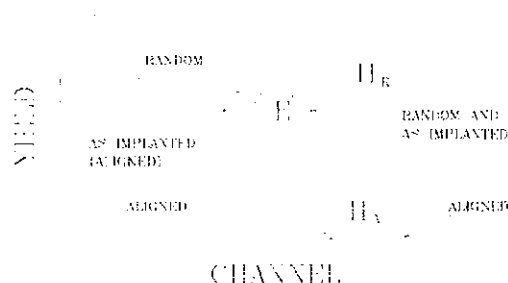


**Figure 22.** Typical RBS spectra for a randomly oriented and axially aligned Sb implanted Si crystal. Spectra from as-implanted (surface damaged) and annealed samples are shown.

lattice. Such atoms can occupy either substitutional or interstitial sites, as shown in Figure 23, and these will interact in different ways during ion bombardment. If a random spectrum is taken, the yield from foreign atoms will give the total number of atoms present. In the case of channelled spectra, substitutional foreign atoms will suffer a similar drop in yield to the host atoms. However, for interstitial atoms the channelled yield will depend upon the location of the atoms and the direction of channelling. For example, in the case illustrated in Figure 23, body centred interstitials will be 'visible' to the beam in direction (1) but not in direction (2) and the reverse is true for face centred interstitials. Considerable information can therefore be gained on the location of impurity or dopant atoms by measuring channelling yields along a number of different axes or planes.

A common application is in the study of ion implantation doped semiconductors. A typical example is the implantation of Si by Sb ions. As the dopant in Si is usually a heavier element, its RBS signal appears isolated at a higher energy, as illustrated in Figure 22. Three spectra are presented here: random, as-implanted aligned and aligned after annealing to remove implantation damage. The as-implanted aligned spectrum indicates that the surface region of the Si, represented by $\Delta E$, has been heavily damaged and the yield of the Si and implanted Sb which resides within this damaged region is the same as for the random spectrum. Beneath the damaged region the Si yield is higher than for the pure crystal case, because many of the incident ions are scattered in the damaged surface layers to angles beyond the channelling critical angle. When the sample has been fully annealed and the crystal structure restored, the Si yield matches that of a channelling spectrum from a defect free crystal and the Sb yield is also shown to have dropped considerably. If the number of counts in the random (or as-implanted) Sb peak is $(Sb)_R$ and the number of counts in the aligned and annealed Sb peak is $(Sb)_A$, then it can be shown[15] that the fraction of Sb atoms sitting on substitutional or shielded sites in the annealed sample is given by

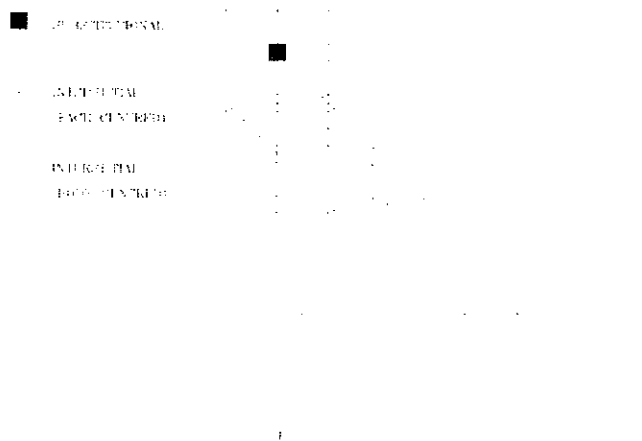$$N_{sub} = \frac{1 - (Sb)_A/(Sb)_R}{1 - \chi_{min}}.$$ (17)



Figure 23. A schematic of a crystal containing substitutional (■), face centred interstitial (X) and body centred interstitial atoms (□). Substitutional atoms are not 'visible' to the beam in any channelling direction whilst face centred interstitials only are visible in direction (2) and body centred interstitials only in direction (1).
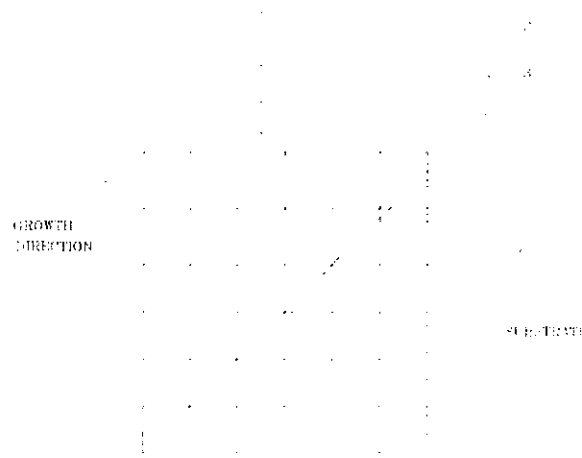


Figure 24. Schematic showing how epitaxially grown layers with lattice parameter mis-matched to the substrate result in tetragonal distortion along the growth direction.

If measurements are made on the samples at various stages in the annealing process, the level of damage remaining and the changes in location of dopant atoms can be studied as a function of time or annealing temperature.

Since the development of molecular beam epitaxy many crystalline materials have been successfully grown on suitable crystal substrates. Indeed it is now possible to grow thin layers of defect free crystals which are lattice mis-matched with the substrate and in which the strain is taken up by tetragonal distortion, as illustrated in Figure 24. One such class of materials are strained layer superlattices where thin layers are built up under alternating compressional and tensional strain, thus altering band-gaps and giving the possibility of engineering new types of semiconductor. Another class are thin layer epitaxially grown superconductors which may also be under strain. It is clear from Figure 24 that channelling performed in the growth direction will reveal a perfect crystal, provided the strain is not sufficient to produce dislocations. Because of the tetragonal distortion of the surface layer, however, chanelling along another channel will be sensitive to the degree of distortion and careful measurement of the channelling angles will enable the degree of distortion to be measured for the surface layer. Analysis of strained layer superlattices where a large number of different alternating layers may be involved is a much more complex situation involving 'resonant channelling' and 'catastrophic dechannelling'. More detailed information on these subjects can be found in the paper by Picroux et al[16].

## 4. Experimental equipment

**4.1. Accelerators.** Probably the majority of accelerators currently being used for energetic ion beam analysis started their life as nuclear structure facilities. However, accelerators are now being purchased in increasing numbers specifically for use in materials analysis. As depth resolution is directly related to beam energy resolution, accelerators used are generally confined to dc machines which are capable of producing beams with energy spreads in the range 0.05–0.2%. Terminal voltages from a few hundred kilovolts to several million volts are used and beam currents up to a few microamps are produced. Because such high potentials are required, accelerators are placed inside a pressure
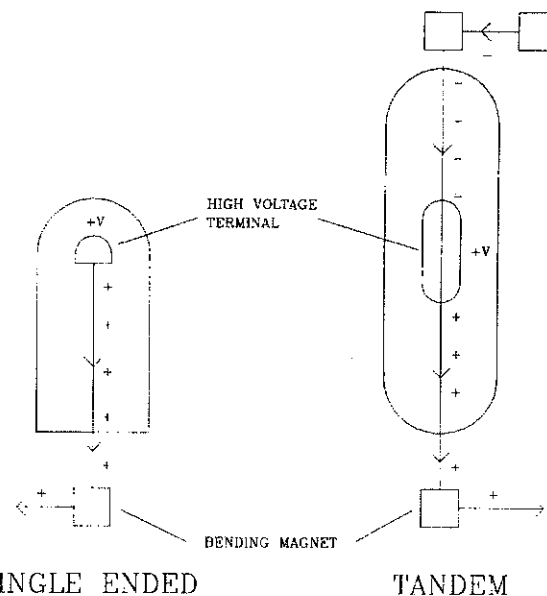
**Figure 26.** A 1 MV electrostatic accelerator dedicated surface analyser capable of producing 3 MeV helium beams. (Photograph courtesy of Electrostatics International Inc., ref 18.)

vessel containing electrically insulating gas at high pressure ($SF_6$ is the most effective insulator). Accelerators consist of an ion source which injects ions into an evacuated beam tube containing a graduated electric potential which accelerates the ion. Various steering, focusing and bending elements are provided and the high energy beam is directed into the sample through a set of collimating apertures which accurately define the beam size and position. The vacuum in the beam line is kept better than 100 $\mu$Pa. Calibration of the energy of the beam is carried out by reference to various well known nuclear resonance or threshold energies; examples being the 991.87 keV $^{27}$Al$(p, \gamma)^{28}$Si resonance and the $^{13}$C$(p, n)^{14}$N threshold at 3235.7 keV. A more detailed description of the design of various accelerators is given in Krane[17] and a list of the energy of useful calibration reactions and thresholds is given in table 2.7 of ref 9.

Direct current accelerators are generally of two broad types. In those using the Van de Graaff principle, charge is transported mechanically to an enclosed high voltage terminal where it is collected to produce a voltage $V = Q/C$, where $Q$ is the charge on the terminal and $C$ is the terminal capacitance. Charge is either sprayed into an insulating belt, or more probably induced onto conductors separated by insulators and connected to form a continuous moving chain. It is then picked off at the high voltage terminal. The other class of dc accelerator is based on the rectification of an oscillating voltage and uses a series of rectifiers and capacitors in the form of voltage doublers (as in Cockcroft–Walton machines). The simplest design of accelerator, known as single-ended, places the ion source within the high voltage terminal at potential $V$ and singly charged positive ions are accelerated to an energy of $V$ electron volts. A useful alternative, known as a tandem accelerator, places the ion source outside the pressure vessel and at ground potential and accelerates negative ions to the high voltage terminals at potential $V$ volts. At this point the beam is passed through on thin carbon foil or narrow canal containing low pressure gas which strips electrons from the ion, giving it a positive charge. The positive ion is then accelerated back down to ground potential and acquires a total energy of $(n + 1)V$ electron volts where $n$ is the number of positive charges on the ion after being stripped in the terminal. These two approaches are shown schematically in Figure 25. The advantages of the tandem configuration are that the ion source is outside the pressure vessel, allowing easy access for maintenance, and a lower high-voltage can be used, leading to a smaller diameter accelerator and softer X-rays from the terminal. A commercially available 1 MV tandem accelerator dedicated surface analyser[18] capable of producing 3 MeV helium beams is shown in Figure 26.

### 4.2. Target stations.

A schematic of a typical target station is shown in Figure 27. Samples are mounted in the centre of a cylindrical vacuum chamber and a beam spot about 1 mm square is defined by a collinating aperture just before the chamber. When channelling measurements are being undertaken, a parallel beam is defined geometrically using a second 1 mm square aperture a further 3–4 m back along the beam line. Also, in channelling measurements the sample is mounted on a triple axis goniometer which allows the sample orientation to be varied about each of the three axes in steps of 0.01°. For routine investigations many samples can be mounted on a target ladder or carousel and moved into the beam for analysis by remote control without having to break the vacuum system.



SINGLE ENDED          TANDEM

**Figure 25.** Schematic diagram of a single-ended and tandem electrostatic accelerator.

In some applications the sample may be very large, or may contain moisture or other volatile materials. For such cases it is possible to bring the beam out of the vacuum chamber, through a thin window onto the sample, which is usually surrounded in an inert atmosphere of helium.

For most samples it is sufficient to maintain a vacuum in the chamber of 100 $\mu$Pa or better, because the depth profiling capability of ion beam analysis enables contributions from surface contamination to be avoided. Ultra-high vacuum is sometimes required however. In such cases it is often sufficient to simulate uhv conditions by providing local liquid-nitrogen-temperature cryo-pumping. For absolute measurements, accurate integration of the beam charge is also important. As energetic positive ions produce secondary electrons, it is important to provide suppressor electrodes both near the aperture before the chamber, to prevent electrons entering the chamber, and near the sample to prevent the escape of electrons from the sample. In some cases, charge is collected from the whole target station which then acts as an enclosed Faraday cup. Charged particle detectors are placed inside the vacuum chamber at appropriate angles to the incident beams. Gamma ray and neutron detectors, however, can be placed outside the chamber, although maximum detection efficiency requires short sample to detector distances.
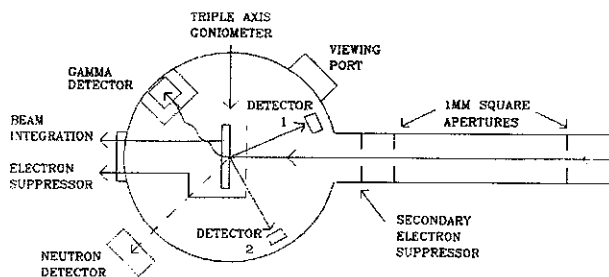


**Figure 27.** Schematic plan of a typical ion beam analysis target station.

**4.3. Ion microprobes.** Many samples contain inhomogeneities with dimensions as small as a micron or less and it is often necessary to use very high spacial resolution for an accurate analysis. The first attempts to produce ion microprobes used very fine collimated beams[19,20]. Great problems were experienced with vanishingly small beam currents and with halo produced by slit-edge scattering. These problems were greatly relieved when Cookson et al[21] used a relatively large object slit and focused the beam to a small spot using strong focusing lenses. Excellent reviews of the development and application of ion microprobes can be found in an article by Cookson[22] and a book by Watt and Grime[23].

Mega electron volt ion beams are rather rigid and not easy to deflect. It is therefore necessary to employ strong focusing elements, such as magnetic quadrupole lenses, to focus them effectively. Various arrangements of lenses have been used[22], ranging from two to four quadrupoles. Such systems, which may not be symmetric in the $X$ and $Y$ planes, produce demagnifications typically in the range 5–30 and can produce beam spots less than one micron square. One of the advantages of ion microbeams is that the beam suffers only a small lateral expansion with depth, so that a 1 $\mu$m diameter beam can be used to profile to a depth of several microns without significant loss of lateral resolution.

Microbeams can be employed in several ways. In the most common mode, the beam is scanned rapidly over a sample in a raster pattern and the energy of the nuclear interaction products are recorded individually, together with their $XY$ locations, and the data is stored sequentially in a computer memory. On completion of the measurement the data is sorted according to each $XY$ location, allowing a spectrum to be reconstructed for each point. Potentially huge volumes of data can be accumulated and this is often reduced by storing only pre-selected portions of the energy spectrum. An alternative approach is to allow the beam to remain at a selected position on the sample, whilst a spectrum is built up. The disadvantage of this method is that the extremely high power densities in such small sample volumes can produce severe damage. Microbeams are also ideal for producing STIM images and very small beam spots can be used as only very low count rates are required.

**4.4. Detectors and electronics.** The electrical signal from most radiation detectors is very small and requires considerable amplification. In addition, counting rooms are often a considerable distance from the target station. Charge sensitive preamplifiers are therefore placed very close to the detectors to minimise cable capacitance and minimal pulse shaping and modest amplification allows the signal to be transmitted by coaxial cable to the counting room. At the counting station the signal is further amplified with appropriate pulse shaping to optimise the energy resolution and pulse length (around 1 $\mu$s) to reduce pulse distortion by overlap of successive pulses (pile-up). Pulses are amplified in the range up to 10 volts and are digitised by an analogue-to-digital converter and stored in a dedicated microcomputer in 512 or 1024 'bins' or 'channels'. All electronics used are commercially available and are fully described by Knoll[24] and Leo[25].

The majority of detectors used for ion beam analysis are based on Ge or Si semiconductors and consist of reverse biased rectifying junctions. Such solid-state devices have the advantage of requiring a low energy to produce an electron–hole pair and thus have a good energy resolution. Silicon is used for charged particle detectors, producing compact detectors with 100% intrinsic
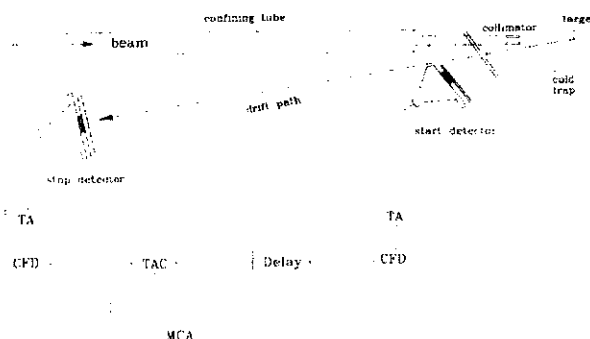


**Figure 28.** Schematic experimental arrangement of a heavy ion time-of-flight energy analyser. TA: timing amplifier; CFD: constant fraction discriminator; TAC: time-to-amplitude convertor; MCA: multi-channel analyser. (Reproduced by permission of M Dobeli et al, ref 26.)

efficiency which operate satisfactorily inside the vacuum system at room temperature. The energy resolution (full-width-at-half-maximum) can be as small as 11 keV for alpha particles but is considerably higher for heavy ions; being as high as 100 keV for 40 MeV oxygen ions and 300 keV for 50 MeV sulphur ions[24]. Annular detectors are available which provide large solid angles at backward angles with the beam passing through the centre of the detector before striking the sample. These offer high efficiency whilst not suffering from large-angle kinematic broadening. An energy resolution an order of magnitude higher can be provided by magnetic spectrometers. However, these have very small solid angles and require separate measurements at each energy setting, leading to very long measurement times with increased beam damage of the sample. The improved mass resolution of heavy ion RBS can be realised if the energy of the ions can be measured with good resolution. Döbeli et al[26] have developed a time-of-flight system using micro channel plates to amplify the electron signal produced when the ion passes through a thin carbon foil at the beginning and end of a known flight path. A schematic of their detector is shown in Figure 28 and part of the RBS spectrum of 25 MeV $^{35}$Cl ions backscattered from a 55 nm GaAs layer on SiO$_2$ is shown in Figure 29. The two gallium peaks are from the two naturally occurring isotopes $^{69}$Ga and $^{71}$Ga. The width of the peaks is due almost entirely to the layer thickness clearly
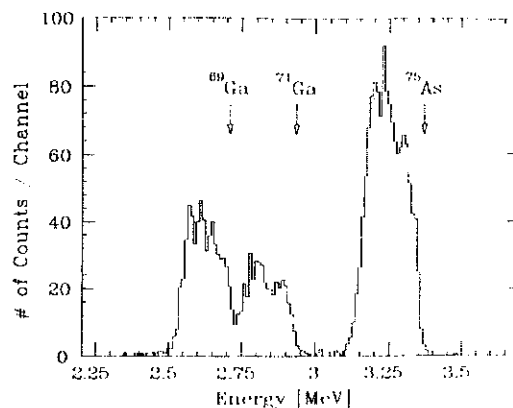


**Figure 29.** 25 MeV $^{35}$Cl backscattering from a 55 nm GaAs layer on SiO$_2$. Masses 69, 71 and 75 are clearly resolved. (Reproduced by permission of M Dobeli et al, ref 26.)

indicating the superior depth and mass resolution. The main disadvantages of time-of-flight systems are their relative complexity and low solid angle. For gamma ray detection, Ge detectors are preferred, as they can be produced with a larger active volume, and the photoelectric cross-section is about 60 times larger than that for Si. However, the smaller band gap necessitates operating Ge detectors at liquid nitrogen temperature to reduce noise. The high resolution of Ge detectors, about 0.15% at 1.33 MeV, makes them ideal for analysis where many gamma energies are present. When only one or two gamma lines or high energy gammas are present, NaI (Tl) scintillation counters are often preferred as they have a much higher detection efficiency than Ge detectors. The energy resolution is much poorer at the same energy, however, at around 8%.

## 5. Applications

Rutherford backscattering and nuclear reaction analysis have found extremely wide application in the analysis of the near surface of materials from a very wide range of disciplines. As it is not possible to cover the range adequately, this section aims to take examples from just three areas to illustrate the diversity of information obtainable from energetic ion beam analysis.

### 5.1. Semiconductors.
In the field of semiconductor technology $SiO_2$ is an important dielectric used for isolation of components and its location, thickness and composition is of great importance. One approach to producing buried oxide layers is to implant silicon to a very high dose with energetic oxygen ions, which then form an insulating $SiO_2$ layer around the end of their range, leaving a surface layer of pure silicon. Figure 30 shows the particle spectra obtained when 900 keV deuterons were used to bombard a 1.3 $\mu$m layer of thermal oxide on silicon and a buried oxide layer produced by oxygen implantation[27]. The small peak in channel 680 is from the (d, p) reaction with a thin surface layer of carbon and the peaks in channels 540 and 340 are from the $(d, p_0)$ and $(d, p_1)$ groups from $^{16}O$. The broader group centred around channel 580 is from the $^{16}O(d, \alpha_0)^{14}N$ reaction. Inspection of the latter clearly indicates a thin buried $SiO_2$ layer and computer simulation analysis reveals the composition shown in the inset in Figure 30. There is evidence for a thin interface layer above the oxide which is deficient in oxygen and this is thought to be due to oxygen diffusion into the damaged region of the Si crystal just before the end of the range of the implanted oxygen
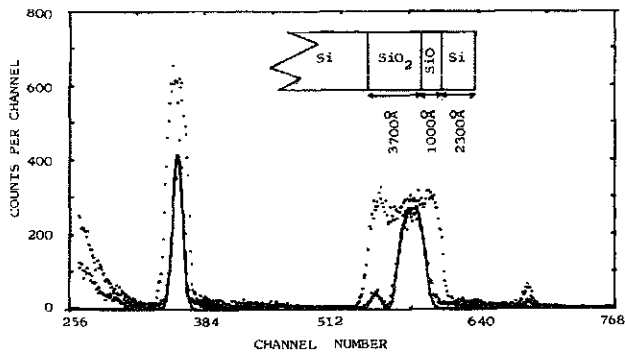
**Figure 30.** Energy spectra of particles emitted from the 900 keV deuteron bombardment of samples of (a) $SiO_2$ on silicon and (b) oxygen implanted silicon. The smooth curve shows the simulation from the implanted sample assuming the structure shown in the inset[27].
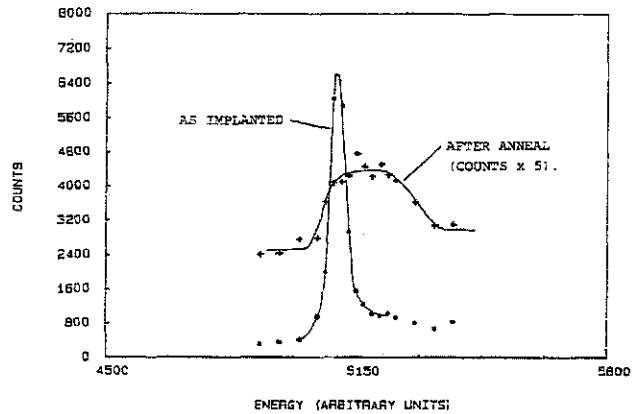
**Figure 31.** The yield curves of the $^{19}F(p, \alpha\gamma)$ reaction around the 882 keV resonance energy for samples of $^{19}F$ implanted $SiO_2$ before and after annealing under dry nitrogen at 1090°C (ref 28).

ions. The buried layer is found to be 370 nm thick with a depth resolution of 200 nm and is stoichiometric $SiO_2$.

Following a suggestion that the presence of fluorine in $SiO_2$ improves radiation hardness, $^{19}F$ was implanted into an oxide layer and its behaviour with annealing was studied with the $^{19}F(p, \alpha\gamma)^{16}O$ reaction using the 882 keV resonance[28]. Figure 31 shows the resonance yield curve for a 600 nm thick oxide layer which had been implanted with $^{19}F$ ions to a dose of 1E 19 m$^{-2}$. The shape of the sharp resonance curve is dominated by the resonance width of 4.7 keV for the as-implanted sample. However, after the sample had been annealed in dry nitrogen at 1090°C for one hour, the fluorine, as indicated by the broad resonance curve, had redistributed uniformly throughout the oxide layer and nearly half had been lost from the surface.

### 5.2. Surface engineering.
Many materials have advantages such as strength, ease of engineering processing, low cost and often low weight. However, they can also suffer from disadvantages such as poor corrosion resistance, poor wear properties and a high coefficient of friction. Surface engineering aims to alter the surface properties of otherwise advantageous materials to make them more widely useable[29].

Probably the most common approach is to treat surfaces in various ways with nitrogen. One such procedure is to subject a surface to a nitrogen-atmosphere-plasma glow discharge where the accelerated nitrogen ions interact with and heat the surface, resulting in the formation of a nitrogen-rich layer with a deeper nitrogen diffusion tail. Such a process forms a hard coating which adheres well to the surface. In the following example, commercially pure (CP) titanium was treated in a 485 V plasma containing 90% N and 10% Ar atoms and was analysed by alpha particle RBS and deuteron NRA[30]. Figure 32 shows the 2 MeV He$^+$ RBS spectra measured at a laboratory angle of 150° for untreated and plasma treated CP titanium, where it is seen that the top 0.25 $\mu$m has been converted to $\delta$TiN, with a further micron converted to $\epsilon$Ti$_2$N. An analysis was not possible beyond 1 $\mu$m depth. Of interest is the presence of surface traces of Cu and Fe which originate from sputtering of the plasma chamber components. The contamination extends to a depth of 15 nm and contains 0.15% atoms of Fe and 0.08% atoms of Cu. Near the surface, where the nitrogen concentration is changing rapidly, a depth resolution of 10 nm is achieved. Nitrogen analysis to
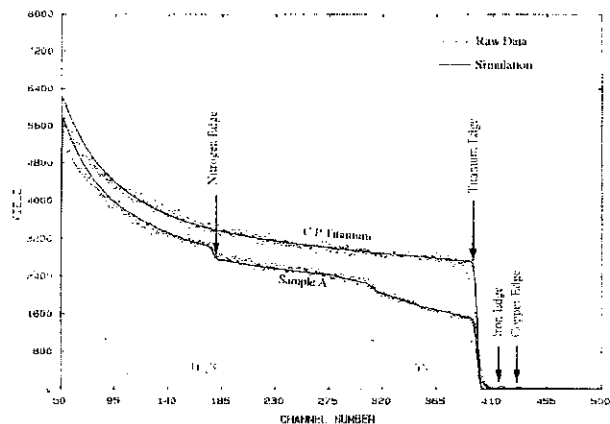
Figure 32. 2 MeV He⁺ RBS spectra of CP titanium and plasma nitrided CP titanium. The smooth lines are computer simulations. Two small surface peaks corresponding to iron and copper are also visible[30].



Figure 34. The nitrogen depth profile produced from the combined RBS and NRA measurements shown in Figures 32 and 33 (ref 30).

greater depths was carried out by observing NRA products from 1.1 MeV deuteron bombardment at 150 . A 12 μm Al absorber foil was used to eliminate scattered deuterons and the resulting spectrum is shown in Figure 33. Peaks can be seen arising from the $^{14}N(d, p)^{15}N$ and $^{14}N(d, \alpha)^{12}C$ reactions and from (d, p) reactions with small amounts of carbon and oxygen contaminants. The insert to Figure 32 shows a detail of the $^{14}N(d, p_{1, 2})^{15}N$ peaks, together with a computer simulation of the data. The nitrogen depth distribution determined from the NRA was then combined with the surface data from RBS to produce the nitrogen concentration depth profile shown in Figure 34. It can be seen that the top 0.25 μm has formed a somewhat over-stoichiometric and rapidly varying δTiN layer, followed by a further
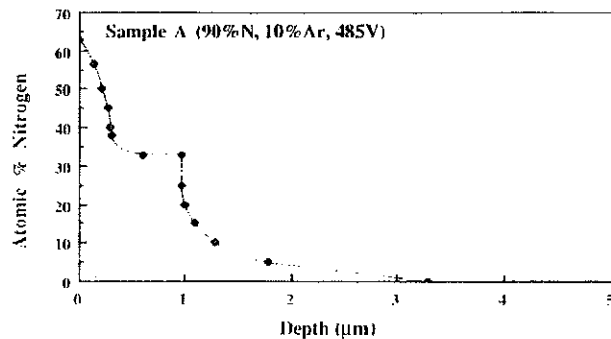
0.75 μm of εTi₂N, beneath which is a long tail of diffused nirogen to a depth of approximately 3 μm.

In an alternative treatment, steel was coated with a thin layer of Zr, which was then covered with a layer of ZrN produced by sputter coating[31]. The total layer measured approximately 4 μm and was too thick to be analysed by conventional RBS. In this case, the sample was analysed using 2.2 MeV deuterons, detecting reaction products at 135 . No absorber foil was used and both deuteron RBS and NRA particles were observed as shown in Figure 35. A computer simulation of the elastic scattering is shown in Figure 36. The data indicated 1.43 μm of ZrN on top of 2.25 μm of Zr over a steel substrate. The layer was seen to be uniform in composition with no interdiffusion at the interfaces. The data suggested slightly over-stoichiometric nitride. Figure 37 shows computer simulations of the $^{14}N(d, \alpha_0)^{12}C$ and $^{14}N(d, \alpha_1)^{12}C$ contributions, again indicating 1.43 μm of ZrN. A deuteron energy of 2.2 MeV was chosen to take advantage of the relatively slowly varying cross-section around this energy. Two
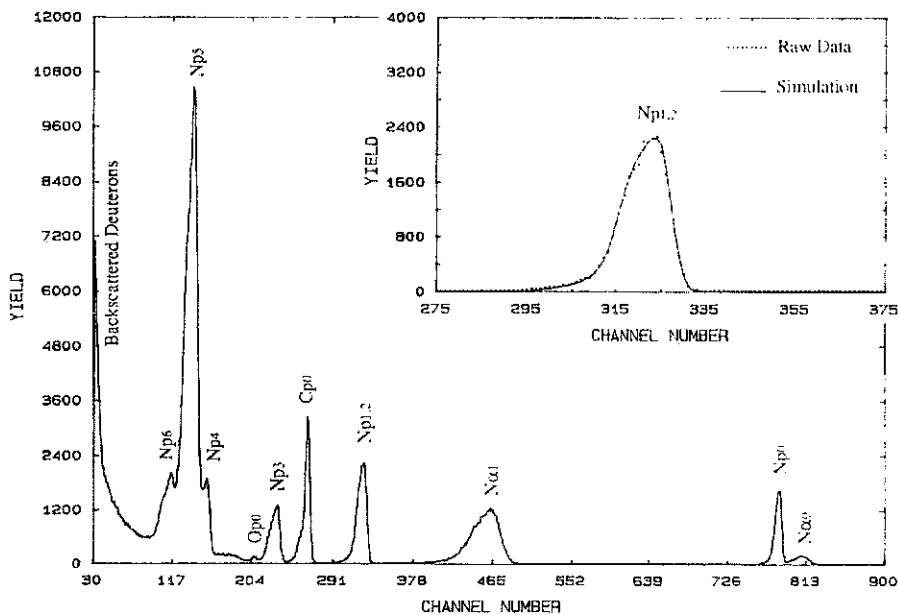


Figure 33. NRA spectrum from the 1.1 MeV deuteron bombardment of plasma nitrided CP titanium using a detector placed at 150 covered with a 12 μm Al absorber foil. The Np₁,₂ peak has been expanded in the inset to show the computer simulation used for depth profiling[30].

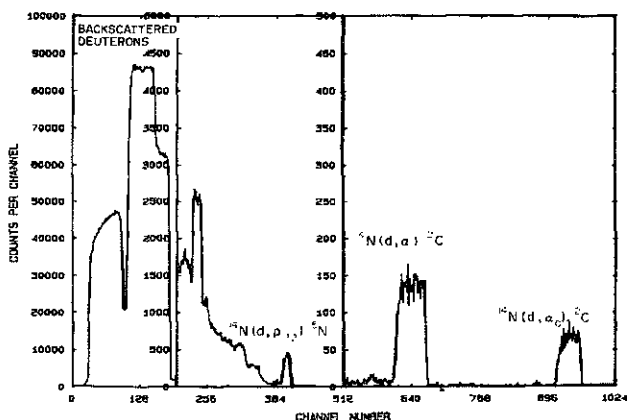**Figure 35.** The energy spectrum of particles emitted at 135° from the 2.2 MeV deuteron bombardment of a ZrN/Zr coating on steel[31].
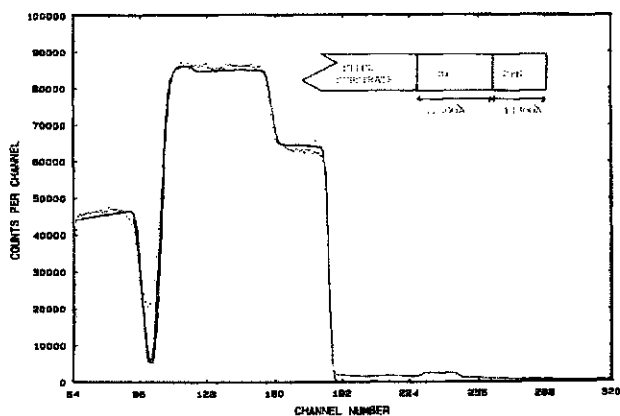


**Figure 36.** The portion of the spectrum shown in Figure 33 corresponding to backscattered deuterons. The smooth curve is the simulated spectrum for the layer structure shown in the inset[31].
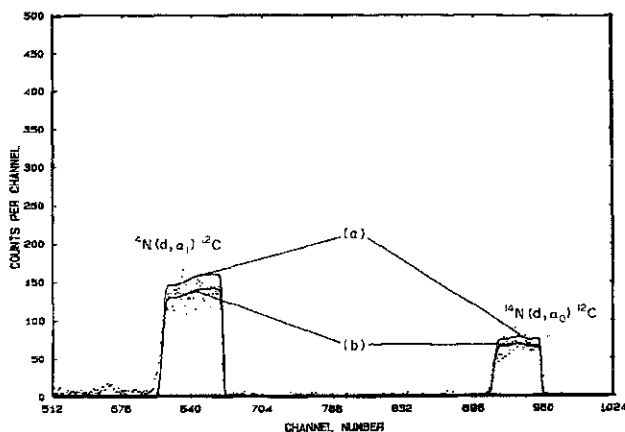


**Figure 37.** The portion of the spectrum shown in Figure 33 corresponding to the $^{14}N(d,\alpha_0)^{12}C$ and $^{14}N(d,\alpha_1)^{12}C$ reaction products. The smooth curves are simulations corresponding to (a) a 1.43 $\mu$m ZrN layer and (b) the best fit to the data corresponding to 12% less nitrogen[31].

simulations are shown. Curve (a) is for 1.43 $\mu$m of ZrN and curve (b) is for a layer containing 12% less nitrogen. The uncertainty in the $(d, \alpha)$ cross-sections however, is also about 12%.

**5.3. Superconducting films.** Thin film superconductors are widely manufactured by epitaxy on crystalline substrates. These tend to have superior properties to bulk superconductors, are an important medium with which to study fundamental properties, and also have particular application in the field of electronic devices.

A wide range of approaches to superconductor film epitaxy have been investigated and ion beam analysis techniques have provided valuable support during this development phase. Figure 38 shows a 2 MeV $He^+$ RBS spectrum, measured at 150° of a $YBa_2Cu_3O_7$ (YBCO) superconductor film grown by rf sputtering at 650°C onto a MgO substrate in a partial pressure of oxygen[32]. This particular sample was produced at an early stage in the development of the technique when the relative proportion of the metals could vary greatly during film growth. The smooth line through the data is the best fit computer simulation and the contribution from each metal is drawn separately for clarity. It can be seen that the Ba content starts low and falls over the first third of the layer, then rises rapidly to a constant level, Yr is relatively uniform throughout the film, except for a large drop for a short period near the middle, and the Cu content starts high and falls steadily to zero at the surface. This spectrum illustrates the insensitivity of RBS to oxygen in a heavy matrix and also highlights the need for computer simulation techniques to extract information in complex situations.

In a separate set of experiments, YBCO films were grown on (001) MgO by *in situ* electron beam co-evaporation in the presence of atomic oxygen and were analysed by $He^+$ RBS and channelling measurements[33]. RBS spectra taken with 2 MeV $He^+$ RBS at 150°, together with $\langle 001 \rangle$ axis channelling data for two thin films with slightly different composition, are shown in Figure 39. The sample in Figure 39(a) was measured to have a thickness of 330 nm and a stoichiometry of Y : Ba : Cu of 1.25 : 1.78 : 2.97. The excellent computer fits to the random spectrum indicate uniform distributions and a sharp interface with the MgO. The channelling spectrum has a $\chi_{min}$ for Ba of 8%, indicating a very high degree of crystallinity in the film. The sample in Figure 39(b)
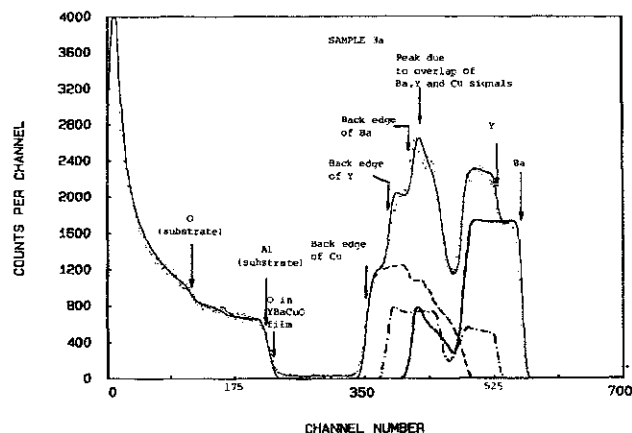


**Figure 38.** The 2 MeV $He^+$ RBS spectrum from a rf sputtered YBCO film on a MgO substrate. The smooth curve through the points is a computer simulation and the contributions from the individual elements in the film are shown for Ba (solid line); Y (dash–dot line) and Cu (dashed line)[32].
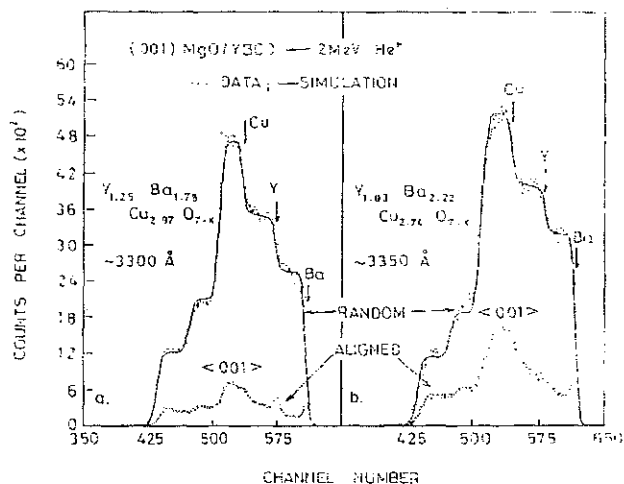
801

CHANNEL NUMBER

**Figure 39.** The random backscattered and channelled spectra for 2 MeV He⁺ RBS from (a) 330 nm of $Y_{1.25}Ba_{1.78}Cu_{2.97}O_{7-x}$ on MgO. and (b) 335 nm of $Y_{1.03}Ba_{2.22}Cu_{2.74}O_7$ on MgO. The smooth lines through the points are computer simulations[35].



ANGLE FROM < 001 > DIRECTION (DEG)

**Figure 40.** The axial angular yield curves of 1.5 MeV He⁺ RBS taken through the ⟨001⟩ and ⟨103⟩ directions along the {010} plane for the sample shown in Figure 39(a). The inset depicts the ⟨001⟩, ⟨103⟩ and ⟨101⟩ directions in an unstrained YBCO film on a MgO substrate[35].

was found to have a Y : Ba : Cu ratio of 1.03 : 2.22 : 2.74. Here the computer simulation of the data (assuming a uniform composition) is not perfect near the interface and this indicates a small composition gradient of 5%, increasing in Cu and Y towards the interface. The channelling spectrum has a $\chi_{min}$ for Ba of 14%, indicating that this crystal does contain defects.

These superconducting films have a rather large lattice parameter mismatch with MgO : the value for MgO being 4.21 and that for the YBCO being 3.82. It is expected, therefore, that the layers will be strain relieved at a thickness of 300 nm. Angular channelling scans along the {010} plane for Mg and Ba around the ⟨001⟩ axis and for Ba around the ⟨103⟩ YBCO axis are shown in Figure 40. The angular difference is 44.6 , which is entirely consistent with an unstrained film with appropriate lattice parameters $a = 3.82$ and $(1/3)c = 3.89$.

## 6. Conclusions

An attempt has been made in the previous sections of this chapter to introduce the range and power of RBS and NRA as near-surface analytical techniques. In the last few paragraphs, therefore, the more important features will be summarised and one or two future developments outlined.

Taken together, RBS (including ERDA) and NRA provide for the essentially non-destructive analysis and depth profiling of all elements in the periodic table in the near-surface of materials. In the case of RBS, measurements are accurate (3–5%) and quantitative and do not require the use of secondary standards. The same applies for selected isotopes for NRA and is true, in general, when standards are also employed. In addition, the depth profiling capability allows accurate measurements to be made just beneath the surface, thus avoiding the undesirable effects of surface contamination. The sensitivity of the techniques depends on such experimental parameters as the beam charge, detector efficiency and solid angle. The examples quoted in the following paragraphs are therefore typical values only and are subject to variation in individual cases.

Rutherford backscattering has a high cross-section and analyses are fast, typically taking between 5 and 30 min. Depth pro-
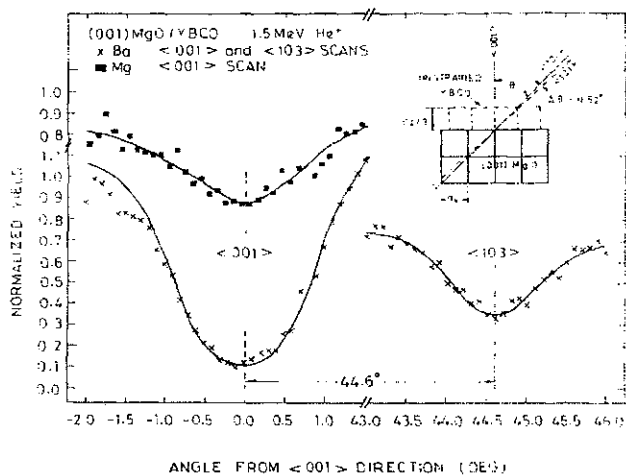
filing is possible between 10 nm and 1 μm and measurements can distinguish between consecutive masses up to about mass 45 for 2 MeV ⁴He beams. This limit can be pushed much higher by using high energy heavy ions and elaborate detecting systems. The Rutherford cross-section has a $Z^2$ dependence. Hence sensitivities as high as 10⁻³–10⁻⁴ monolayers are possible for heavy elements (10⁻¹–10⁻³ for light). The technique is relatively insensitive to light elements in a heavy matrix. However, considerable advantage can often be gained in these cases by taking advantage of enhanced non-Rutherford cross-sections, although lack of precision of the cross-section values leads to the dependence on standards for absolute determinations. Up to 5–10 elements can be measured simultaneously with a depth resolution as high as 1 nm at the surface to 40 nm at depth. Straggling dominates the depth resolution for thicknesses greater than 100 nm. Taken in conjunction with ERDA, all elements in the periodical table can be measured. ERDA can measure hydrogen to 1000 ppm atoms or 0.1 monolayers and when coincidence techniques are employed the sensitivity can be reduced to as low as 1 ppm atoms.

Nuclear reaction analysis complements RBS extremely well, measuring all elements from hydrogen to sulphur with good sensitivity. This is especially advantageous for many light elements which are difficult to measure by other techniques. Sensitivities depend on individual reaction cross-sections and range from % to 100 ppm in advantageous cases and < 1 monolayer. Depth resolution ranges from 2–20 nm, again depending on the reaction. NRA is a very complex technique in execution and interpretation and requires a high level of experience in the selection of appropriate reactions, detection angle and ion beam energy. A maximum of 2–3 elements can be satisfactorily measured simultaneously. The maximum analysis depth is around 10 μm. Cross-sections are smaller than most RBS values and measurement times tend to be longer, around 15–30 min each. Accurate absolute measurements are possible for selected isotopes. However, most measurements are made relative to standards. One of the major assets of NRA is that reactions are isotope specific and measurements can often be made of different isotopes of the same element, thus elucidating chemical reaction processes (e.g. $^{12}C/^{13}C$, $^{14}N/^{15}N$, $^{16}O/^{18}O$).

Both RBS and NRA, when used in conjunction with channelling, provide valuable information on crystalline materials. Analysis along different planes and axes reveal impurity atom locations. Crystal integrity can be studied, providing information on defect and damage depth profiles, and the fraction of implanted or impurity atoms in substitutional sites can be determined. For epitaxially grown layers, crystal integrity, lattice strain by tetragonal distortion and changes in lattice parameter can all be measured to high accuracy.

Current advances in the field include the development of new detector systems, enabling advantage to be taken of the better surface mass separation with heavy ion beams, and the use of enhanced non-Rutherford cross-sections for the analysis of light elements. Considerable efforts are now being made to make accurate measurements of many of these non-Rutherford cross-sections. Another area of advance is the development of better microprobes with sub-micron beam spot sizes. The current push is towards 100 nm resolution. Even higher resolutions are possible with STIM imaging, which requires very few particles to form an image. In conclusion, it may be safely said that, although RBS and NRA are now mature technologies, much new and exciting development work is still being undertaken.

## References

[1] H Geiger and E Marsdon, *Phil Mag*, **25**, 604 (1913).

[2] E J Rutherford, *Nature*, **103**, 415 (1919).

[3] S Rubin, *Phys Rev*, **78**, 83 (1950).

[4] S Rubin, T O Passell and L E Bailey, *Anal Chem*, **25**, 736 (1975).

[5] Electrostatics International Inc., Box 310, Middleton, Wisconsin, USA.

[6] W K Chu, J W Mayer and M A Nicolet, *Backscattering Spectroscopy*. Academic Press, New York (1978).

[7] L C Feldman, J W Mayer and S T Picraux, *Materials Analysis by Ion Channeling*. Academic Press, New York (1982).

[8] L C Feldman and J W Mayer, *Fundamentals of Surface and Thin Film Analysis*. North Holland, New York (1986).

[9] J R Bird and J S Williams, *Ion Beams for Materials Analysis*. Academic Press, Australia (1989).

[10] G Demortier (Ed), *Proc Third International Conf Microanalysis of Light Elements (Hydrogen to Neon) using Charged Particle Accelerators*. *Nucl Instum Meth*, **B66**, 1 (1992).

[11] J B Marion and F C Young, *Nuclear Reaction Analysis Graphs and Tables*. Academic Press, New York (1968).

[12] H W Lefevre, R M S Schofield, G S Bench and G J F Legge, *Nucl Instrum Meth*, **B54**, 363 (1991).

[13] R M S Schofield, H W Lefevre, J C Overley and J D McDonald, *Nucl Instrum Meth*, **B30**, 398 (1988).

[14] J F Zeigler (Ed), *The Stopping and Ranges of Ions in Matter*. Pergamon Press, Oxford (1972), (1980) and (1985).

[15] W A Grant, In *Methods of Surface Analysis* (Edited by J M Walls). Cambridge University Press, Cambridge (1989).

[16] S T Picroux, W K Chan, W R Allen and J A Ellison, *Nucl Instrum Meth*, **B16**, 306 (1986).

[17] K S Krane, *Introductory Nuclear Physics*. Wiley, New York (1988).

[18] Photograph courtesy of Electrostatics International Inc., Graber Road, Box 310, Middleton, WI 53562-1310, USA.

[19] T B Pierce, P F Peck and D R A Cuff, *Nature*, **211**, 66 (1966).

[20] B K Mak, J R Bird and T M Sabine, *Nature*, **211**, 738 (1966).

[21] J A Cookson, A T G Ferguson and F D Pilling, *J Radioanal Chem*, **12**, 39 (1972).

[22] J A Cookson, *Nucl Instrum Meth*, **165**, 477 (1979).

[23] F Watt and G W Grime (Eds), *Principles and Applications of High-Energy Ion Microbeams*. Adam Hilger, Bristol (1987).

[24] G F Knoll, *Radiation Detection and Measurement*. Wiley, New York (1989).

[25] W R Leo, *Techniques for Nuclear and Particle Physics Experiments*. Springer, Berlin, Heidelberg (1987).

[26] M Döbeli, P C Haubert, R P Livi, S J Spicklemire, D L Weathers and T A Tombrello, *Nucl Instrum Meth*, **B56/57**, 764 (1991).

[27] J C B Simpson and L G Earwaker, *Nucl Instrum Meth*, **B15**, 502 (1986).

[28] L G Earwaker, M C Briggs, M I Nasir, J P G Farr and J M Keen, *Nucl Instrum Meth*, **B56/57**, 855 (1991).

[29] T Bell, Z L Zhang, J Lanagan and A M Stains, *Surface Treatments for Corrosion and Wear Resistance* (Edited by K N Strafford, P K Datta and C G Cosgrove), Chapter 12. Ellis Horwood, Chichester (1984).

[30] H J Brading, P H Morton, T Bell and L G Earwaker, *Proc Third International Conf Advances in Coating and Surface Engineering and Wear Resistance*, Newcastle, UK (1992).

[31] J C B Simpson, L G Earwaker and M N Khan, *Nucl Instrum Meth*, **B24/25**, 701 (1987).

[32] R S Sokhi, P W Gilberd and L G Earwaker, *Nucl Instrum Meth*, **B50**, 140 (1990).

[33] H Jhans, L G Earwaker, N G Chew, J A Edwards and A G Cullis, *Nucl Instrum Meth*, **B56/57**, 768 (1991).